

SI Appendix, Figure legends

Figure S1. View of south entrance to TPL with excavation area in the lower part of the background. Photo taken from the south, looking towards the north.

Figure S2. Top: Photo of the main gallery of TPL from the cave entrance, looking north. Test pits are shown on the left (trenches 1 and 2); excavation site is shown on the right (trench 3). Bottom: Photo of the main gallery of TPL from the west looking east. Test pits are shown in the foreground (trenches 1 and 2); excavation site is shown in the background (trench 3).

Figure S3. Photo of excavation site at the northeast end of the main gallery of TPL.

Figure S4. Photo of TPL 1 *in situ*. On the right side of the photo, partial maxilla can be seen; on the left, partial frontal bone is visible; parietal is seen in the foreground.

Figure S5. Top: TPL excavation; Bottom: Details of the stratigraphic section of TPL showing an undisturbed stratigraphy. Continuous, horizontal white layer is the powdery, white limestone precipitate (see text).

Figure S6. Plan of the TPL excavation (bottom right). Stratigraphic sections from trenches 1-3 are shown and correlated.

Figure S7. Line drawing of relationship between excavation site (trench 3) and test pits (trenches 1 and 2).

Figure S8. TPL 1 3D reconstruction. Original elements are in blue; duplicated elements are in gold. Left: anterior view. Right top: right lateral view. Right bottom: posterior view.

Figure S9. Comparison of summed anterior (I1-C) and posterior (P3-M2) buccolingual crown diameters (measured in mm) for TPL 1 relative to other Pleistocene samples. TPL 1 has relatively small summed anterior buccolingual tooth diameters relative to archaic human samples (top graph) and relatively large posterior buccolingual tooth diameters relative to all

samples (bottom graph). Each box represents the interquartile range; the horizontal line within the box represents the median value of the data.

Figure S10. An example of OSL and TL dating results for sediments from TPL excavation (sample code TPL3): (A) An OSL shine-down curve for 100 s of blue diode stimulation; (B) Red TL decay curve for 1000 s of isothermal heat at 260°C; (C) OSL dose response curve for single aliquot data; (D) Red TL dose response for the unbleachable (heat-reset) signal; (E) Radial plot of the OSL single-aliquot paleodose distribution presented at 1 σ error. The shaded line represents a 2 σ error range from the central value, calculated using the central age model and incorporates data from 56 accepted aliquots; (F) Red TL dose response of the bleachable (light-reset) signal. Note that the curve starts at the unbleachable paleodose so the bleachable dose response is much flatter than the OSL dose response, resulting in lower precision.

Figure S11. The results of OSL single-aliquot and single-grain analysis for samples TPL1-3 presented as radial plots. The single-aliquot data are presented in the left column (A, C, E) and the single-grain data are in the right column (B, D, F). The shaded area represents D_e values within 2 σ of the central value for each distribution, while the solid line on the single-grain plots represents the D_e value determined using the minimum age model.

Figure S12. An inter-laboratory comparison of single-grain data for sample TPL-3. (A) Single-grain data generated by the dating facility at Gloucester University; (B) Single-grain data from the dating facility at Macquarie University. Distributions and overdispersion values are indistinguishable.

Figure S13. Dose recovery data for all three TPL samples. The recovered D_e values have been plotted for the accepted grains from (A) TPL-1; (B) TPL-2; and (C) TPL-3. The solid line represents the surrogate dose (100 Gy), and the shaded area represents D_e values within 2 σ of the surrogate dose. (D) The accepted grains from all three samples presented on a radial plot with a central value of 99 Gy according to the central age model.

Figure S14. A comparison of linearly-modulated optically stimulated luminescence (LM-OSL) curves. The LM-OSL curve for TPL-3 has been compared with a similar curve from a sample known to contain a dominant fast component (M3T from Lake Mungo in NSW Australia) and a sample known to contain a dominant medium and/or slow component (Pun5 from Punung in East Java) (44). The LM-OSL curves reveal that the TPL OSL emissions are also dominated by a fast component but with a slightly lower luminescence intensity than the Australian sample.

Figure S15. A comparison of red TL glow curves from (a) a laboratory-irradiated aliquot of sample WR1 from Liang Bua in western Flores and (b) a laboratory-irradiated aliquot of sample TPL-1 from Tam Pa Ling northern Laos. Sample treatments are shown in the legend, where 'bleach' denotes bleaching only by visible wavelengths (i.e., deficient in UV). The inset plots show the difference in TL counts between the glow curve measured after preheating and that measured after UV-deficient bleaching and preheating. The resultant plots, therefore, show the temperature region of the glow curve associated with the easy-to-bleach red TL signal, which is most intense at 260-305°C. The comparison demonstrates that despite being of difference intensity the volcanic and granitic quartz display a similarity in peaks and bleaching potential.

SI Appendix, Table legends

Table S1. Radiocarbon dating of four charcoal samples retrieved from TPL as shown on **Fig. 1** (Radiocarbon Dating Laboratory, Illinois State Geological Survey, University of Illinois at Urbana-Champaign, USA.). The half-life of 5568 is used for age calculation. Ages are reported as BP (before present defined as before 1950).

Table S2. U-Th dating of TPL 1¹ (Department of Geology, University of Illinois at Urbana-Champaign, USA).

Table S3. Cranial measurements for TPL 1 and comparative samples. All measurements in mm. Data given as mean \pm s.d. (N). Samples are as follows: W-LA: Western Eurasian late archaic humans; E-LA: Eastern Eurasian late archaic humans; MPMH: Middle Paleolithic modern humans; W-UP: Western Eurasian Upper Paleolithic humans; E-LP: Eastern Eurasian Late Pleistocene humans. For additional information on sample composition see SI.

Table S4. Maxillary crown dimensions of TPL 1 in mm.

Table S5. Red thermoluminescence multiple estimate results.

Table S6. Optically stimulated luminescence single-aliquot rejections.

Table S7. Optically stimulated luminescence single-grain rejections.

SI Appendix

SI Text

I. Excavation history and site summary

The lower part of Pa Hang Mountain was extensively excavated in 1934 by Jacques Fromaget, Chief of the Geological Service of Indochina. At this time, the Tam Hang rock shelter was identified on the southeast face of the mountain, and archaeological and paleontological excavations were undertaken. Middle Pleistocene mammalian fauna were excavated from breccia deposits in the walls and karstic network of the Tam Hang rockshelter (1-3). Archaeological artifacts and human remains dated to ca. 16 ka were recovered from sediments under the shelter (4-7).

Based on Fromaget's publications, the location of Tam Hang was re-identified by Thongsa Sayavongkhamdy of the Department of National Heritage, Lao P.D.R. and reopened for study in 2003 by two of the authors (A.-M. Bacon and F. Demeter). The site has been excavated by several of the authors annually since 2006 (A.-M. Bacon, F. Demeter, P. Düringer, T. Sayavongkhamdy, L. Shackelford). The goal of the 2006 project was to document the presence of the first human settlements in the region through continued excavation at Tam Hang and extensive survey of the surrounding area for additional fossil localities. While surveying the Pa Hang Mountain in November 2008, P. Düringer and J.-L. Ponche discovered Tam Pa Ling (TPL) cave. At this time, three test pits were excavated on the floor of the cave: trenches 1 and 2 on the west side of the cave and trench 3 on the east side of the cave (Fig. S2). Charcoal samples from trench 3 were collected in November 2008 and radiocarbon dated at the Illinois Geological Survey in January 2009 (see below). Based upon AMS radiocarbon dates, trench 3 was opened as the primary excavation site at TPL during the next field season (December 2009), at which time the human remains were discovered and additional sediment samples were collected for luminescence dating.

Stratigraphy and sedimentology

The floor of the main gallery of TPL lies at the base of a steep, 65 m-long slope. The 30 m-length of the gallery is oriented in a north-south direction; its 40 m-width is oriented in an approximately east-west direction. The stratigraphy and sedimentology of the cave were examined in the primary excavation (trench 3) at the east end of the cave and followed across the gallery and correlated with test pits on the west side of the cave (trenches 1 and 2) (Fig. S2).

Analysis of the TPL trenches identified three main types of sediments: sandy clays from TPL 1; silty clays from TPL 2 and a calcite-rich argillaceous layer close to the powdery limestone precipitate layer of TPL 3. The dark reddish brown sediments sampled in the middle and upper part (0-3 m) of the filling sequences of TPL 1 and TPL 2 are characterized by limestone clasts, calcite and quartz together with iron-oxides, goethite (FeO(OH)), hematite

(Fe₂O₃), and gibbsite (Al(OH)₃). The calcite is derived from the surrounding limestone, while the quartz, clays and secondary iron oxides are derived from outside the cave. Due to the small number of sinkholes present in this cave environment and the stratigraphy and morphology of the cave, it is assumed that the source area for these sediments is the front (south-facing) entrance of the cave. The sample located below the calcitic floor of TPL 3 is similar in composition, but richer in calcite.

The mineralogical assemblage of clay fraction (<2 μm) does not vary significantly between samples. The clay fraction is predominantly made of vermiculite and kaolinite. Vermiculite is interlaid with a small fraction of a hydroxyl-Al component. Minor quantities of illite and fine quartz (sand and silt fraction) also occur alongside the sesquioxides. Vermiculite and kaolinite are widespread clay minerals in soils and weathering profiles and, when associated with iron and aluminum oxides, indicate hydrolyzing leaching conditions (humid sub-tropical climate) that are characteristic of "ferralsols-nitisols" strongly weathered soil types (8). Furthermore, the two main clay minerals, vermiculite and kaolinite, could indicate the mixing of parent sources for the soil components that formed the cave deposit. Kaolinite is a common weathering by-product of a wide variety of parent rocks, including limestone, whereas vermiculite is more often the result of biotite or illite-bearing rocks, such as the surrounding arkose and sandstone parent-rocks found close to the studied outcrop or in Pleistocene karst breccias. With the exception of powdery limestone precipitate, which is linked to a hiatus in the sedimentary deposition, the input of the mineralogical phases does not appear to vary through the span of time.

The composition is predominantly silty clay but it is dispersed with sandy silt layers that contain sand-sized grains within. The sediments represent periodic, local slopewash deposition that has formed distinct and regular layers throughout the sediment column. There is no evidence of rapid deposition; instead the layers alternate between fine and slightly coarser fractions that probably reflect summer and winter influxes of sediment. There is no evidence of bioturbation, post depositional mixing, slumping or reworking, and the preservation of distinct layers suggests minimal disturbance since burial. The sedimentary bedding of all three pits is rigorously parallel to the dip of the soil of the cave, indicating that despite being deposited by slopewash after burial, the sediments and associated fossils have been undisturbed (Figs. S5, S7).

The stratigraphy shows a strong chronological hiatus in the upper part of the section as shown in figure 1, with 46 ka (OSL) below (e) to 2.77 ka (AMS¹⁴C) above (f). This gap could have several origins: a drastic change in the climate approximately 46 ka with a decrease in slopewash activity; a strong increase in slopewash activity that eroded part of the upper units within the last few thousand years before the new sediments were deposited approximately 2.77 ka; or a change in the cave entrance morphology (open or closed) that conditioned the slopewash activity. Due to the lack of an erosion contact between the lower and upper parts of the section, we favor the latter interpretation.

II. Comparative materials for analysis of human remains

Sites yielding specimens providing comparative morphological data for Table 2, Table S3 and Fig. S9.

1. Western Eurasian late archaic humans (W-LA: European + SW Asian Neandertals): Amud, Ang-Angl, Arcy-Bison, Arcy-Hyene, Arcy-Renne, Aubesier, Boccard, Camine, Carihuela, La Chapelle-aux-Saints, Châteauneuf-sur-Charente, Combe Grenal, Dederiyeh, Fenera, La Ferrassie, Forbes' Quarry, Genay, Guattari (Circeo), Hortus, Kebara, Krapina, Kůlna, Marrillac, Monsempron, Montmaurin, Le Moustier, Neander Valley, Palomas, Petit-Puymoyen, La Quina, Saccopastore, St. Brelade, St. Cesaire, Sala, Shanidar, Spy, Tabun, Vindija.

2. Eastern Eurasian late archaic humans (E-LA : Asia – LAH): Changyang, Dingcun, Maba (Mapa), Tongzi, Xujiayao, Zhoukoudian Locality 4.

3. Middle Paleolithic modern humans (MPMH): Herto, Qafzeh, Skhul.

4. Western Eurasian Upper Paleolithic humans (W-UP): Arancio, Arene Candide, Aurensan, Bacho-Kiro, Brassempouy, Barma Grande, Badger, Bedhillac, Brno, Bruniquel, Calanca, Cap Blanc, Cisterna, Cro-Magnon, La Crouzade, Dolní Věstonice, Fossellone, Grotte des Enfants (Fanciulli), Hoteaux, Isturitz, Kent's Cavern, Kostenki, Labatut, Lagar Velho, Laugerie-Basse, Mladeč, Morin, Muierii, Nazlet Khater, Oase, Obercassel, Oetrange, Parpallo, Piage, Roc de cav, Paglicci, Abri Pataud, Pavlov, Předmostí, Les Roches, Rochette, Sandalja, Sunghir, Urtiaga, Veyrier.

5. Eastern Eurasian Late Pleistocene humans (E-LP): Huanglong, Liujiang, Minatogawa, Quingliu, Tapon, Tam Hang, Zhoukoudian-Upper Cave, Ziyang.

III. 3D Reconstruction of TPL

The TPL 1 fossil fragments were scanned with a Siemens Somatom Sensation 16 CT scanner (tube voltage 120 KeV, tube current 330 mA, pixel dimension 0.44 mm, slice thickness 0.7 mm). A 3D reconstruction of the TPL 1 cranium was created from CT scans following established methods using Amira software. When bilateral structures were preserved on one side only, missing portions of the cranium were generated from comparable parts preserved on the original bones. Each reconstructed element was positioned using corresponding anatomical landmarks of a late Pleistocene human cranium from Laos (9) as a model. The frontal was positioned using nasion and the superciliary arches. The parietal was positioned using the preserved sagittal and coronal sutures. The temporal was positioned using porion, the zygomatic arch and the petrous portion of the bone. The occipital was positioned using inion and the partial lambdoid suture. The maxillae were positioned using the nasal floor and the anterior teeth. Although currently unsuitable for a morphometric analysis, this reconstructed skull gives a general idea of the morphology of TPL 1.

IV. Strategy for establishing a chronology

When the cave site was initially discovered and tested in 2009, four charcoal samples were collected from trench 3 for radiocarbon dating (sample depths: 0.4 m, 1.2 m, 2.1 m and 4.3 m). The potential age of the sediments was close to the upper limit of radiocarbon dating so ages of the collected samples (charcoals) were viewed as minimum ages. The TPL 1 human remains were recovered in 2010. Direct ESR/U-series dating of the human teeth was not possible because the material was fixed with a preservative. Instead, a sample was removed from the frontal bone for U-series dating.

Establishing a chronology for the skeletal material at TPL required the use of more than one dating technique; specific depositional circumstances, however, precluded the use of some techniques. For example, useful calcite material could not be found within the sedimentary column. Instead, layers containing a fine white powder or ‘moonmilk’ (limestone precipitate) were discovered. This precipitate does not harden as does a speleothem, making it vulnerable to reprecipitation. Despite its prolific occurrence in the sedimentary layers, its open system behavior renders the deposit inappropriate for U-series techniques. Radiocarbon dating using ABOX or Pyrolysis-Combustion (10) pretreatment would have been preferable but this was hampered by very small charcoal samples. Therefore, additional independent age estimates were required to provide an upper limit to the timing of sediment deposition and to discount the possibility that the radiocarbon results represented older charcoal that had been washed into the cave. Luminescence dating is the most appropriate and useful sediment-based dating technique for establishing the time since the quartz grains were last exposed to sunlight thus a range of luminescence techniques were employed. As granitic quartz produces both red and UV emissions (11-14) a dual signal approach could be employed whereby both red thermoluminescence (TL) dating of the red emissions and ultraviolet (UV) optically-stimulated luminescence (OSL) dating of single-aliquots and single-grains were analyzed as an internal test of paleodose consistency (15).

Luminescence techniques (both TL and OSL) measure the time at which sediments were either last heated (e.g., burnt or fired) (16) or exposed to sunlight during transport or deposition (e.g., by wind or water) (17) via the stimulation of minerals using heat (TL) or light (OSL). These are trapped charge techniques whereby a light sensitive signal or energy is “trapped” in defects in the crystal lattice of minerals such as quartz and feldspar. This energy slowly builds up and is stored in the crystal during a period of burial in the sediment column. The amount of trapped energy is proportional to the amount of naturally occurring ionizing radiation found in the surrounding sediment and the amount of exposure time during the burial period (16). This signal is reset to zero by sunlight so it acts as a clock that measures the time since last exposure (18). This makes these techniques unique amongst dating methodologies as they can be used to estimate the time elapsed since sediments were buried (19). These depositional ages represent an extremely desired commodity in paleoanthropological research since most processes or events are based on the deposition of sediment.

V. Luminescence dating methods

Sedimentary context and sampling strategy

The composition is predominantly silty clay but it is dispersed with sandy silt layers that

contain plenty of sand-sized grains within the 90-212 μm size range to be employed for dating. Samples for luminescence dating were collected at 2.35 m (the level of the TPL 1 cranial remains) and 3.15 m to bracket the age range of deposition. An additional sample was collected at the base of the excavation (at that time) to provide a basal age for the sediment column and to investigate the rate of sedimentation in the cave (4.2 m). The association between the sediments and fossils is clear; all fossils were discovered *in situ* with little evidence of bioturbation, sedimentary mixing or post-depositional modifications. The stratigraphic integrity of the site has been maintained despite periodic slopewash entering the cave. The sediments contain no evidence of cut and fill processes, channels being eroded or large erosion contacts, suggesting that the water from slopewash processes remains on the surface and does not interfere with the underlying sedimentary layers. As such, the radiocarbon age estimates should provide a minimum age for fossil deposition, the red TL age estimates a maximum age (see later discussion) and the UV OSL single-aliquot and single-grain age estimates should provide a result close to the 'true' burial age.

Sample collection and preparation

Bulk sediment samples (laboratory code TPL1-3) for luminescence dating were collected from a cleaned exposure of the TPL excavation using a cover and red filtered torch light for illumination and then stored in a light-safe container. Additional samples of sediment were collected from within 30 cm of the TL/OSL sample and subsequently combined for water content and environmental radioactivity determinations. Quartz grains of 90–125 μm in diameter were separated from the matrix under dim red illumination using standard purification procedures, including a final etch in 40% hydrofluoric acid for 45 minutes to remove the external alpha-dosed rinds (16). The acid-etched 90–125 μm grains were mounted on stainless-steel discs using silicone oil spray as adhesive with a total area of either 7 mm (red TL) with each aliquot being composed of ~5000 grains, 0.5 mm (OSL) with each aliquot being composed of ~50 grains, or 180-212 μm sized single-grains of quartz loaded on aluminum discs for OSL single-grain analysis.

A. TL dating

Although northern Laos is not a volcanic province per se, it is surrounded by volcanic regions to the south in Sumatra and Indonesia, to the east in the Philippines and to the west in Burma. As such, these sediments may have been influenced at some point in the past by large-scale volcanic events. This, combined with the estimated antiquity of the material and the need for an internal check on the consistency of the luminescence results, warrants the use of the red TL signal for dating. Aliquots were analyzed using a modified SAR protocol (20) to isolate the light-sensitive red TL signal (21). The dual-aliquot protocol (DAP) described in detail in (21) was originally designed to exploit the intense red TL emissions typical of quartz from a volcanic province (22-27). Using this technique, the time elapsed since the quartz grains were last exposed to sunlight was obtained from the light-sensitive (bleachable) component of the red TL signal. The procedure also determines the time elapsed since the unbleachable signal was last reset by a major heating event such as a volcanic eruption (or being located within a close proximity to heated products such as lava). However, investigations into the spectral emissions

of quartz from different geological settings have revealed that granitic (a form of plutonic) quartz also produces strong and reproducible red emissions (27-29). When the potential for applying the DAP technique to these non-volcanic (non-heated) sediments was explored using a granitic quartz from Australia (PJIES-75 from Purijarra rockshelter, Northern Territory), it was discovered that the red TL results were comparable with independent age estimates from OSL single-aliquot, SL single-grain and radiocarbon techniques (30). This result implies that despite being designed specifically for volcanic quartz, DAP measurement conditions are also appropriate for granitic quartz and this is supported by the results of dose recovery tests (see later section). Furthermore, recent investigations into quartz emissions have revealed that strong red and UV emissions are a feature of granitic quartz (15) and that both emissions can be used to provide an internal check on the consistency of the equivalent dose (D_e) (31). Therefore to accommodate the lack of 'heating' history – aliquot A is described as the hard-to-bleach TL residual level that is only reset by very long bleaching periods (>1 week, which rarely occurs in cave environments) (27), while its subtraction from the aliquot B signal isolates the easy-to-bleach signal that is used to estimate the timing of sediment deposition.

Therefore, the DAP was used to exploit the intense red TL emissions typical of granitic quartz (11-14). Using this technique, the time elapsed since the quartz grains were last exposed to sunlight may be obtained from the light-sensitive (bleachable) component of the red TL signal. Aliquots were heated to 260°C at a heating rate of 5 K s⁻¹ and then held at 260°C for 1000 s to minimize the unwanted TL from incandescence. Paleodoses were estimated from the 20–30 s interval of isothermal decay (which was bleachable by >380 nm illumination), using the final 160 s as background. As tests of protocol performance, the regenerated OSL dose-response curve included a zero-dose point to measure the extent of thermal transfer and a duplicate regenerative dose point to examine the adequacy of the test dose sensitivity-correction procedure.

Equipment

The isothermal red TL emissions were measured using a red sensitive photomultiplier tube (Electron Tubes Ltd 9658B) and cooling tower (LCT50 liquid-cooled thermoelectric housing) with Kopp 2-63 and BG-39 filter combination, and laboratory irradiations were conducted using a calibrated ⁹⁰Sr/⁹⁰Y beta source. The use of these isothermal measurements rather than traditional glow curve measurements (incorporating heating up to 450°C) reduces the potential signal loss from thermal quenching (32) and the potential for temperature induced sensitivity changes (33, 34). D_e were estimated from the 20–30 s interval of isothermal decay (which was bleachable by >380 nm illumination) using the final 160 s as background. The isothermal red TL emissions were measured using a red sensitive photomultiplier tube (Electron Tubes Ltd 9658B) and cooling tower (LCT50 liquid-cooled thermoelectric housing) with Kopp 2-63 and BG-39 filter combination (26), and laboratory irradiations were conducted using a calibrated ⁹⁰Sr/⁹⁰Y beta source.

Error

The uncertainty on the D_e includes random errors (including photon-counting errors, errors associated with the variance in the background signal, instrument reproducibility, and errors

associated with D_e determination derived by Monte Carlo simulation (35)), systematic errors (including a 2% error for beta source calibration) and total errors (the quadratic sum of the random and systematic errors). The precision is much lower for red TL dating in comparison to OSL due to the use of dual aliquots. This technique requires the errors to be propagated through from the first to the second aliquot resulting in precisions of up to ~30 %. However, when compared to independent dating techniques across a suite of different samples the accuracy of the DAP technique is comparable (36, 37).

Recovering a known dose – red TL

The ability to recover a known dose from a sample when tested is a useful indication of the suitability of the procedures and experimental conditions employed (20), especially in this sedimentary context where there is little independent age control. Therefore, dose recovery experiments were conducted initially on fresh aliquots to select appropriate procedures and secondly on used aliquots to provide a crude test of the procedures employed. The natural signal was removed from the fresh aliquots using minimal heat treatments so as not to cause any sensitivity change between the surrogate natural and first regenerative cycles. Fresh aliquots were stimulated isothermally (heated to 260°C and held for 1000 s) to erase the natural signal associated with the red TL emissions. Fresh aliquots were bleached in a solar simulator light box for a short duration (1 hour) only to remove the easy-to-bleach signal but maintain the hard-to-bleach signal, and a dose was administered to induce a regenerated easy-to-bleach signal. The aim was to recover this signal using a range of preheat and isothermal measurement conditions ranging from 220-280°C. In addition, a used sample was given a small, known dose (e.g., 50 Gy) followed by a bleach, and then a second, larger dose (e.g., 100 Gy). Thus, the relative size of the doses used to fill the hard-to-bleach and easy-to-bleach source traps were known (e.g., 150 and 100 Gy) and attempts to recover these doses were made using the previous methodology. In general, the conditions that recovered a dose closest to the given dose and that produced an acceptable dose-response curve were taken to be most appropriate for that sample and indicated that the luminescence signal could be measured reproducibly under controlled experimental conditions. The results of the dose recovery tests indicated that the standard 260 preheat and isothermal measurement combination are also appropriate for these samples and that by using these conditions the surrogate dose could be recovered to within 10%. This result agrees with previous dose recovery procedures using DAP on a range of samples (21, 30) and was replicated using the 6 used aliquots.

The precision is much lower for red TL dating in comparison to UV OSL due to the use of dual aliquots. This technique requires the errors to be propagated through from the first to the second aliquot resulting in precisions of up to ~30 %. However, when compared to independent dating techniques the accuracy of the DAP technique is comparable (29). DAP requires a minimum of two aliquots to determine the bleachable D_e . To minimize any complications arising from differences in material properties between aliquots A and B and to improve the signal to noise ratio, we used large aliquots composed of many grains. However, not all of these grains are likely to have been fully bleached when last transported, therefore the bleachable TL ages should be viewed as maximum ages for sediment deposition (21). Representative data is

displayed in Fig S10. DAP was originally designed for samples with minimal amounts of quartz, hence the use of only two aliquots (21). However samples containing more quartz allow multiple determinations of the aliquot A and B D_e to test the range of D_e present using 12 aliquots. Unfortunately the low red light levels emitted by single-grains of quartz prevent the use of small aliquots or single-grain techniques to analyze the distribution of paleodoses from single-grains, but the use of multiple estimates of the paleodose will at least determine whether the results are reproducible and assess the distribution of paleodoses between aliquots. These estimates are presented in Table S5 and demonstrate a D_e range for each sample that is close to the original dual aliquot estimate. This result indicates that the inter-aliquot variability is small and despite the use of only two aliquots, the use of the DAP technique facilitates a relatively close approximation of the ‘true’ D_e . If the minimum age model (38) is applied to these multiple estimates, the D_e value is reduced by 7-11 Gy and is closer to the OSL D_e estimates. Although still representing maximum D_e values, these results indicate that the lower dose aliquots contain a smaller proportion of partially bleached grains. These data have also been included in the final results table (Table 1).

B. OSL dating

To improve the confidence in the final age estimate, to provide an internal check on D_e consistency and to determine the likely extent of any TL age overestimation arising from incomplete bleaching of quartz grains at the time of sediment deposition, the UV OSL signal was also measured using a modified single-aliquot regenerative-dose protocol (39-41). Acid-etched 90-125 μm grains were loaded onto stainless steel discs (12) using a 0.5 mm mask and the ultraviolet emissions were detected by an Electron Tubes Ltd 9235QA photomultiplier tube fitted with 7.5 mm of Hoya U-340 filter. A calibrated $^{90}\text{Sr}/^{90}\text{Y}$ source was used to perform laboratory irradiations delivering a dose rate of 7.877 Gy/min for stainless steel discs. The single-aliquot regenerative dose protocol (SAR) (20) was employed for all UV OSL measurements. This revolutionary technique uses paired measurements (a natural/regenerative and a test dose measurement) to account for the sensitivity changes induced by the regenerative cycles of bleaching, dosing and heating. The most robust tests of the procedures employed for the SAR measurements is the dose recovery test for internal consistency and preheat plateau test to determine optimum preheat conditions.

Recovering a known dose – OSL signal

Dose recovery experiments were also conducted on fresh aliquots to select appropriate procedures and on used aliquots to test the procedures employed. The natural signal was removed from the fresh aliquots using minimal heat treatments so as not to cause any sensitivity change between the surrogate natural and first regenerative cycles. Fresh aliquots were bleached (using blue diodes at 50% power for 200 s at 50°C) to erase the natural signal. In general, the most appropriate dose for a given sample was considered to be the one that returned the dose closest to the surrogate natural and that produced an acceptable dose-response curve, thus indicating that the luminescence signal could be measured reproducibly under controlled experimental conditions. A beta dose similar to the estimated natural (e.g., 100 Gy) was administered to represent a surrogate natural dose, and an attempt was made to recover this value using a modified SAR protocol. For each aliquot, a different preheat temperature was employed

starting at 200°C for 10 s and increasing in 10°C increments up to 270°C all with a 160°C cut heat after each test dose cycle to determine which preheat conditions recovered a dose closest to the given dose. These results formed the basis of a preheat plateau test. It was determined that the 260°C preheat for 10 s recovered a dose closest to the surrogate natural as was located on the ‘preheat plateau’ so this was chosen as the most suitable preheat condition. These tests also indicated that a hot optical wash treatment was required after every regenerative cycle to remove a thermally transferred component that causes a recuperated signal >5%. Dose recovery tests were also conducted on used single-grains of quartz (see below).

Single-aliquot analysis

Quartz grains in the size fraction 90-125 µm were preheated to 260°C for 10 s (and a cut heat of 160°C after the test dose) and then heated to 125°C and optically stimulated using blue diodes for 100 s, followed by a hot optical wash at 260°C for 100 s to eliminate the recuperation effect. The most light-sensitive component of the OSL signal was obtained from the initial 3.2 s of stimulation (1-8 channels), and the background count rate was estimated from the last 20 s (200-250 channels). As tests of protocol performance, the regenerated OSL dose-response curve included a zero-dose point to measure the extent of thermal transfer and a duplicate regenerative dose point to examine the adequacy of the test dose sensitivity-correction procedure. For each sample, paleodoses were estimated for ~41 out of the 48 aliquots processed. The rejected aliquots were discarded according to the criteria outlined in (41) and listed in Table S6. The statistical overdispersion of the resulting paleodoses was significantly below 20% for all three samples (15, 10, 11%, respectively). However, we speculate that the low overdispersion was a product of the high doses that are nearing (but have not yet reached) saturation. This has truncated the distribution in the upper range so it may not accurately reflect the true distribution of paleodoses. Therefore, to rule out this likelihood we deemed it necessary to further investigate this distribution using single-grains of quartz. We have presented the single-aliquot data to present a complete record of the analysis (Figs. S10, S11) but this data is not included in the final age estimates and is derived solely from the single-grain analysis.

Single-grain analysis

The TL-DA-20 Risø unit containing the single-grain attachment was utilized for all OSL single-grain analyses. The attachment was used in combination with custom-made aluminum discs containing 100 precision-drilled 300 µm (depth and diameter) holes in a ten-by-ten grid (39, 42). A calibrated ⁹⁰Sr/⁹⁰Y source was used to perform laboratory irradiations at a dose rate of 10.92 Gy/min for the aluminum single-grain discs. Detailed single-grain analysis of the beta source using calibration quartz (4.81 Gy batch 60 from Riso) revealed slight variations in the spatial homogeneity of the source ranging from 8.7-12.8 Gy/min, so dose rate corrections for each hole were applied to the generated D_e values. Each of the 180-212 µm sized quartz grains was stimulated for 2 s using a 10 mW 532 nm Nd:YV0₄ solid-state diode-pumped green laser, which was focused to deliver 50 W/cm² of power to a 20 µm-diameter spot, and the ultraviolet emissions were detected by an Electron Tubes Ltd 9235QA photomultiplier tube fitted with 7.5 mm of Hoya U-340 filter. The most light-sensitive component of the OSL signal was obtained from the initial 0.12-0.3 s of stimulation (6-15 channels), and the background count rate was estimated from the last 1.62-1.9 s (81-95 channels). The single-grain data have been presented as

radial plots in Figure S11 alongside the single-aliquot data for comparative purposes.

Most of the single-grain measurements were conducted at the luminescence facility at Macquarie University. Additional measurements were conducted at the OSL facility at the University of Gloucester UK (approximately 500 grains per samples) to establish an inter-laboratory comparison of single-grain data. Similar measurement conditions were employed and a comparison of the results indicates little or no variation in the distribution of grains (see Fig. S12) therefore the data sets were combined (Fig S11). In total, the OSL paleodoses of 3600 individual grains were measured using a modified single-aliquot regenerative-dose protocol described in detail elsewhere (40, 43). The same preheat conditions as described for the single-aliquot analysis were employed along with a hot optical wash (280°C blue diodes stimulations for 100 s) and two extra regenerative cycles to assess the IR component of each grain.

Recovering a known dose - OSL of single-grains

Similar dose recovery tests were performed on used single-grains of quartz to test the procedures employed. A dose of 100 Gy was administered as the surrogate natural and the same SAR protocol was employed as described for the single-grain analysis. Out of the 100 grains measured the surrogate natural was recovered to within 10-15% for between 10-18 grains with an average of 99 Gy and an overdispersion of 4% (Fig. S13).

Single-aliquot and single-grain rejection criteria

Single-grains were accepted and rejected according to the criteria of (41). In the preliminary analysis a linear fit was used and grains were rejected if the test dose error exceeded 10% and/or the signal was greater than 3σ above the background value. This initial pass also provided recycling and IR ratio values (the ratio of two final SAR regenerative cycles, one incorporating an IR bleach and one without) that could then be utilized for further rejections. Grains were rejected if the associated recycling ratios were greater than 10% either side of unity or if there was greater than 2σ difference between the IR and non-IR regenerative signals. This provided a range of grains that could then be analyzed individually using Analyst. Further rejections were implemented for supersaturating grains, grains dominated by an ultrafast component, grains that displayed recuperation exceeding 5%, excessive increasing or decreasing sensitivity changes in the test dose responses in relation to the natural, the presence of a desensitizing slow component that displays a difference between the natural and first regenerative decay curve, and the dominance of a medium component in the shape of the natural shine down (Table S6).

Modern day analogue

A modern sample (TPL-MOD) was collected from directly outside the cave entrance in a location which afforded partial exposure to sunlight. This area is thought to be the source for the sediments inside the cave and therefore provided a useful location to test the assumption of luminescence dating that most of the grains being brought into the cave were bleached prior to deposition. Once processed using the same methods as described above, the sample was analyzed using both the UV OSL signal (12 small aliquots) and the red TL signal (1 aliquot A and B as per the DAP technique and 5 multiples of aliquot B). The OSL emissions returned an age range of between 0.2-1.5 Gy suggesting that some of the sediment is being bleached before

entering the cave – but due to the nature of the deposition by slopewash processes there is still a strong likelihood that some of the grains have only been partially bleached. The red TL emissions returned an aliquot A D_e of ~400 Gy, which represents the hard-to-bleach component of the red TL signal. However, the aliquot B signal (which represents the isolated easy-to-bleach signal) returned low D_e values of between 0.5-2 Gy. These results indicate that the period of sunlight exposure outside the cave was sufficient to bleach most of the OSL signal and the easy-to-bleach red TL signal but not to reset the hard-to-bleach red TL signal. It is assumed that the hard-to-bleach signal requires much longer exposure times.

Characterizing the nature of the emissions using LM-OSL

To characterize the nature of the luminescence emissions a 10mW green (532 nm) laser was used for linearly modulated (LM) optical stimulation. This allows the separate components of the emission to be identified and provides information that contributes to establishing the integrity of the D_e . Quartz grains were heated to 125°C and then optically stimulated by steadily increasing the laser power from zero to 90% over a period of 30 s. The most light-sensitive component of the LM-OSL signal was obtained from the initial 5 s of laser stimulation, and the background count rate was estimated for the same time interval from a second laser stimulation following each OSL measurement. The background-subtracted LM-OSL stimulation curves were then compared with samples known to contain a dominant fast component e.g., M3T from Lake Mungo in NSW Australia, and samples known to contain a dominant medium and/or slow component e.g., Pun5 from Punung in East Java (44) (example provided in Fig. S14). The LM-OSL curves reveal that the OSL emissions are dominated by a fast component, which vindicates the use of the SAR protocol and confirms that this quartz type emits a UV emission that is suitable for OSL analysis. A detailed analysis of these curves also indicates the presence of a few grains that contain an ultrafast component or contain a dominant medium and/or slow component. Grains containing the latter undesirable OSL components (unsuitable for SAR) have been removed from the single-grain distribution via the rejection criteria.

Estimation of the paleodose using statistical models

The single-grain distribution indicates that the sediment contains a mixture of higher and lower dosed grains ranging from 95-251 Gy (TPL1), 102-286 Gy (TPL2) and 95-303 Gy (TPL3). This distribution could be interpreted as due to a mixing of grains from different layers, small scale variations in the beta dose rate experienced by different grains or a difference in the amount of bleaching time prior to deposition. The opportunity for beta heterogeneity is small due to the small numbers of large limestone clasts (non-radioactive) that could potentially cause ‘cold spots,’ and the homogenous composition of each layer. As deposition is occurring via slopewash processes into a cave environment, the opportunity for incomplete bleaching of each grain makes the latter option the most parsimonious interpretation. It is not unexpected to find partially bleached grains in slopewash, fluvial or colluvial sediments (18); however, the fully bleached grains are the ones that represent the true burial age of the skeletal material. The central age model (CAM) (45) is only suitable for samples that are well bleached, with an overdispersion of less than 20% and is consistent with single-component D_e distributions (43). These samples have overdispersion values of 18.8-21.2%, only slightly higher than the original single-aliquot distribution (10-15%), but the assumption of well bleached may not be accurate

due to the nature of the sedimentary environment. The modern analogue sample from outside the cave entrance returned an age close to zero but there is still a likelihood that some of sediments were deposited rapidly without a period of bleaching in the cave entrance, e.g., during storm events. Therefore, due to the contradictory evidence between the data and our understanding of the depositional environment we have taken the most conservative approach by employing the minimum age model (MAM) (38). This model is sensitive to the presence of low dose grains so the grains that received the most complete bleach will influence the final D_e and therefore provide a depositional age that most closely represents the timing of fossil deposition in the cave. As would be expected the overdispersion of the single-aliquot distribution (10-16%) is lower than the single-grain analysis (~20-22%) due to the averaging effect of multiple grains (46). However, it is interesting to note that the D_e distributions of the single-aliquot and single-grains are surprisingly similar, indicating that despite containing more grains on each aliquot the single-aliquot data still reflect the true distribution of grains. This may also suggest that the samples are not as prone to partial bleaching as first anticipated. Despite this we have still adopted the most conservative approach to interpreting these data and have used only the data derived from the MAM of the single-grains for the final chronology.

The equivalent dose distributions

The samples are not as scattered as would be expected from a typical slopewash or fluvial sediment with a relatively small range of D_e values. This could indicate that only a small degree of partial bleaching has occurred i.e., there is not much difference between the fully bleached and partially bleached grains, and that prior to this depositional event a large proportion of the grains must have undergone a substantial bleaching event. The paleodoses are all stratigraphically consistent and display a clear age-depth relationship. As would be expected the single-grain D_e values are lower than the single-aliquot D_e , and the red TL D_e values are higher than both the OSL results. The agreement between the D_e values for both the UV OSL and red emissions (within the confines of the maximum age constraints for the red TL data) suggest that the results are internally consistent and their agreement with the radiocarbon data provides confidence in the accuracy of the final age from an independent age estimate.

Dose rate

Concentrations of ^{238}U , ^{235}U , ^{232}Th (and their decay products) and ^{40}K were measured by high-resolution gamma spectrometry of dried and powdered sediment samples in the laboratory and a portable gamma spectrometer in the field. It is assumed that the dose rate measured at the time of sample collection has prevailed throughout the burial period. The corresponding (dry) beta and gamma dose rates were obtained using the conversion factors of (47) and the beta-dose attenuation factors of (48), and an effective internal alpha dose rate of 0.03 Gy ka^{-1} was assumed for each sample and included in the total dose rate (49). Cosmic-ray dose rates were estimated from published relationships (50), making allowance for the density and 50 m thickness of the limestone roof above the cave deposit, the geometry of the limestone shielding, the sediment overburden at the sample locality (~2.45-4.20 m), the altitude (~1170 m above sea level) and geomagnetic latitude and longitude (22° and 102°) of the sampling site.

Disequilibrium in the cave environment

High resolution gamma spectrometry of the cave sediments is particularly useful as it provides information on the entire ^{238}U and ^{232}Th decay chains, therefore the concentrations of the daughter as well as the parent nuclides can be explored. This information allows an informed assessment of the state of equilibrium or disequilibrium in this sedimentary environment. As these decay chains contribute to 26% and 27% of the total dose rate (51), disequilibrium in one or both of the chains will have a bearing on the estimated dose rate and age. It is, therefore, important that any excesses or deficiencies in daughter nuclides relative to the parent nuclides are identified and assessed. In this sedimentary environment, three potential disequilibrium states have been identified: 1.) in the ^{238}U chain a deficiency of between 12-40% in ^{226}Ra compared to ^{238}U ; 2.) a ^{210}Pb excess of between 4-14% compared to ^{226}Ra ; and 3.) in the ^{232}Th chain a small excess of between 0.7-2.9% in ^{228}Th compared to ^{228}Ra . Thorium is thought to be immobile in most sediments (88) and this combined with the short half-lives (t) of the daughter nuclides ($^{228}\text{Ra} = 5.7$ yrs and $^{228}\text{Th} = 1.91$ yrs) means that this effect is negligible in samples older than 20 years (51). The excess of ^{210}Pb is probably due to the fallout of lead on surface sediments that are then washed into the cave, but similarly the τ is only 22 years and is unlikely to have any effect on sediments older than 100 years (51). The deficiency in ^{226}Ra could potentially be the most problematic as ^{238}U is more mobile in the sediment column (52), it contributes 27% of the total dose rate and ^{226}Ra has a much longer half-life (1602 years) so any disequilibrium in this chain will affect the accuracy of the final age. This deficiency indicates that radium redistribution is occurring in the sediment column possibly due to the effects of leaching in the cave environment, as suggested by the sediment analysis. However, in a worst case scenario with a ^{228}Ra deficiency of 50% (the sample with the largest deficiency is TPL1 with only 40%) in a closed environment, the deviations from the dose rate are <3% and as ^{238}U contributes 27% of the total dose rate, <3% of the U chain equates to 0.81% of the total dose rate. In addition, if the sediment is buried within a closed environment it will return to secular equilibrium within 30-40 ka which is less than the estimated age of the sample.

However, caves can sometimes act as open environments during the burial period due to the amount of water passing through and the potential for daughter nuclide mobilization. Therefore, the potential disequilibrium from radium mobility is likely to cause a larger deviation than 0.81%, but to determine the true value requires an assessment of whether the sediments were in secular equilibrium at deposition prior to ^{226}Ra leaching from the system or whether the sediments were already in disequilibrium at the point of burial. The Th decay series for these samples is close to secular equilibrium, implying that there has been limited recent mobilization of radium, but the disequilibrium in the concentration of ^{226}Ra indicates that radium has been mobile in the past. To determine the state of the sediments entering the cave and their source an additional sample for dosimetry was collected from the front entrance of the cave. The samples (TPL-FE) contained a similar composition and state of disequilibrium indicating that the sediments have a similar source (as supported by the sediment analysis) and were most probably in disequilibrium upon entry into the cave. This suggests that radium mobility occurred prior to burial. This vindicates the use of high-resolution gamma spectrometry as techniques that only measure the parent nuclides (e.g., NAA and ICPMS) would prove inaccurate. An analysis of the surrounding limestone, arkose and sandstone outcrops as the sources of the clay component (kaolinite and vermiculite) and clasts reveal that the limestone could be the source of the

disequilibrium, which was leached prior to burial in the cave. As the mineralogical assemblage of the clay fraction does not vary between samples, the variation in ^{226}Ra deficiency could reflect the proportion of limestone clasts in the sedimentary layers. The effect of sediments with a prior state of disequilibrium being deposited into a closed system would lead to an error of $\sim 3\%$, and this value would decrease to 0 after 40 ka (53). Alternatively if sediments in disequilibrium are deposited in an open system the error margin would increase to $\sim 6\%$ on the final age estimate (53). The evidence from this site suggests that Thorium redistribution has not occurred and that Uranium mobilization via leaching occurred outside the cave prior to burial. It is however likely that some leaching has also occurred in the cave environment. Therefore to accommodate this additional source of uncertainty the error margin on all the dose rates has been increased by 6% for each sample (according to the findings of (53)).

Estimations of water content

Material collected from around the sampling areas was used for laboratory estimations of the present-day water content. The material was placed in a (pre-weighed) beaker and weighed to determine the wet sample weight. The sample was then dried in an oven at 40°C for several days and reweighed to determine the dry sample weight. Subtracting the weight of the dry sediment and the empty beaker from the original wet sample weight produced a value for the total weight of water loss during drying. The *in situ* water content was then expressed as the weight of water divided by the weight of the dry sediment. These measurements contributed to the assessment of water content variability during the period of burial. In addition, field observations and assessments of past variability were conducted to assist in the final estimation of the annual dose. The total dose rate was calculated using long-term water contents of between $40 \pm 5\%$ and $50 \pm 5\%$, which is close to the measured (field) water content of between 39-59%. We explored the hydrology of the site as a means of understanding the recorded high water content values and discovered that although the site itself was not waterlogged, the sediments (especially the basal sediments) had high water contents – even when sampling in the dry season. Tam Pa Ling shows evidence of water activity e.g., active slopewash and saturated clay deposits. But as the samples were collected during the dry season, it seems reasonable to suppose that the measured water contents represent a value below the annual average. Any present-day assessment of water content must, therefore, represent a minimum value of the long-term average.

Water content variability was assessed according to location, sediment depth and sediment composition. During present-day conditions, northern Laos usually has six wet months and six dry months and is ‘wet’ roughly 55% of the year; Luang Prabang receives about 1,360 mm of rainfall annually. The depths of the samples in the cave environment also influence their water contents, being either covered (e.g., superficial cave sediments that are dry and cracked in the dry season and saturated in the wet season) or deeply covered (e.g., deeply buried cave sediments that are constantly saturated all year round but were once on the cave floor surface). In addition, the composition of the sediment has a bearing on its long-term water content variability; for example, sand tends to drain easily whereas silt and clay absorb water so that the basal silts are in a state of constant saturation. This variability was considered when estimating the errors associated with the water content for each sample to ensure that the errors covered the range of likely values. As a starting point superficial cave sediments would be expected to be

~20 ± 5 % and basal cave sediments ~40 ± 6 %. These values were later modified after including the laboratory estimations of water content. The water content has also been conservatively estimated to accommodate the potential range of water content values of between 40-45%. We attribute these high values to the steep entrance slope and the continuous slopewash processes that channel the surface run-off from the limestone tower down into the cave. This water tends to accumulate in the finer layers as the clays and silts prevent the water from seeping down through the layers.

The TL and OSL ages were calculated by dividing the TL and OSL paleodoses by the corresponding total dose rate (Table 1).

VI. ¹⁴C methods

The standard procedure ABA (acid-base-acid) pretreatment was used for AMS ¹⁴C dating of TPL charcoal samples. The same pretreatment was also applied to the ISGS ¹⁴C-free wood background and wood working standards that include IAEA C5 (Two Creek forest wood), FIRI-D (Fifth International Radiocarbon Inter-comparison D wood) and ISGS Reily AC (about 3 half-life wood) samples.

All samples were weakly boiled for 1 hour in 2M HCl and rinsed to neutrality using DI-water; they were then soaked in 0.125 M NaOH for an hour and rinsed to neutrality using DI-water; subsequently, they were soaked in 2M cool HCl again for 30 minutes and rinsed to pH 6 using DI-water. Samples were dried in an oven overnight at 80°C. About 3-5 mg materials of each TPL charcoal sample and wood background and working standards were placed into preheated quartz tubes for sealed quartz tube combustion at 800°C with minimal amount of Cu (~0.02g), CuO granules (~0.5 g) and a few grains of Ag foil. Quartz tubes were preheated at 800°C for 2 hours, and CuO granules were preheated at 800°C one day before usage. The Cu grains and Ag foils were reduced using hydrogen gas under vacuum at 800°C. The combustion was programmed for 2 hours at 800°C. Then quartz tubes were cooled from 800°C to 600°C for six hours to allow Cu to reduce the NxO to nitrogen gas. The purified CO₂ was collected cryogenically under less than five mTorr vacuum condition for AMS ¹⁴C analysis (10). Purified CO₂ was submitted to the Keck Carbon Cycle AMS Laboratory of the University of California-Irvine for AMS ¹⁴C analysis using hydrogen-iron reduction method (54). A split of purified CO₂ was also analyzed for δ¹³C values using the in-house Finnegan 252 IRMS (isotope ratio mass spectrometer) with a dual inlet device. All results have been corrected for isotopic fractionation according to the conventions of (55), with δ¹³C values measured on prepared graphite using the AMS spectrometer. Sample preparation backgrounds (at least 2 aliquots each time) have been subtracted, based on the measurements of ¹⁴C-free wood blank. The AMS analysis indicated that after background subtraction, wood working standards of IAEA C5, FIRI-D, and Reily AC yielded target values within 1-2σ deviations. We believe that all AMS ¹⁴C assays of TPL charcoal samples represent the true age. The ¹⁴C/C ratio of TPL 09-3 (ISGS A1453) was very close to zero after background subtraction, and the corresponding ¹⁴C age is quoted as a 2σ lower limit.

¹⁴C age conversion (57, 58):

TPL 09-1 (ISGS A1451): 1140 ± 15 ¹⁴C yr BP; 1015 ± 15 cal. yr BP (before 1950).

TPL 09-2 (ISGS A1452): 2770 ± 15 ¹⁴C yr BP; 2865 ± 19 cal. yr BP.

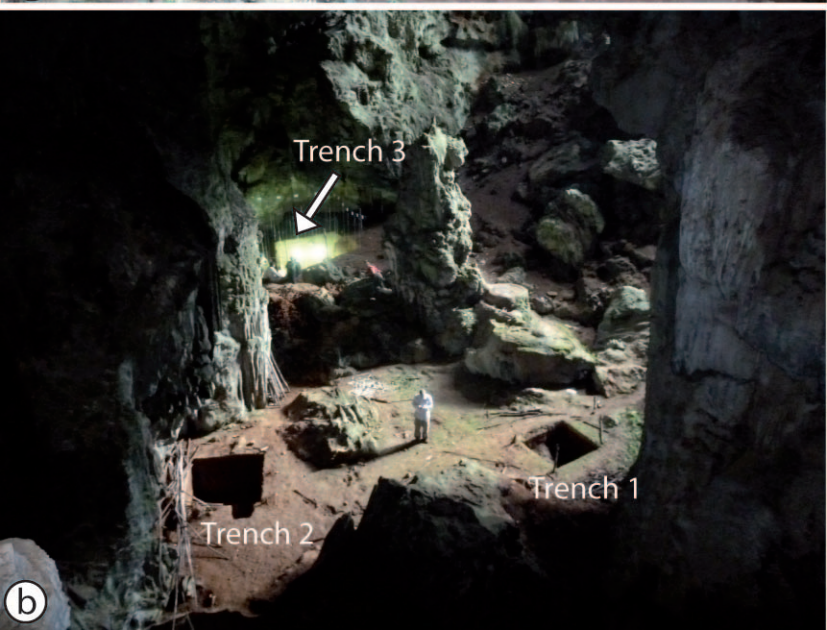
1. Arambourg C & Fromaget J (1938) Le gisement quaternaire de Tam Hang (Chaîne Annamitique septentrionale) [The Tam Hang Quaternary site, Its stratigraphy and its fauna]. Sa stratigraphie et ses faunes. *C R Acad Sci Paris* 203(793-795). French.
2. Fromaget J (1940) La stratigraphie des dépôts préhistoriques de Tam Hang (Chaîne Annamitique septentrionale) et ses difficultés [The stratigraphy of the prehistoric deposits and its difficulties]. *Proc Third Congr Prehistorians Far East, Singapore 1938*:60-70. French.
3. Bacon A-M, *et al.* (2010) The Middle Pleistocene mammalian fauna from Tam Hang karstic deposit, northern Laos: New data and evolutionary hypothesis. *Quat Intl.*
4. Shackelford LL & Demeter F (2012) The place of Tam Hang in Southeast Asian human evolution. *Compt Rendus Palevol* doi:10.1016/j.crpv.2011.07.002.
5. Fromaget J ed (1940) *Les récentes découvertes anthropologiques dans les formations préhistoriques de la chaîne annamitique*. (Government Printer, Singapore), pp 51-59.
6. Fromaget J (1936) Sur la stratigraphie des formations récentes de la Chaîne annamitique septentrionale et sur l'existence de l'Homme dans le Quaternaire inférieur de cette partie de l'Indochine [On the stratigraphy of the recent formations of the Southern Annamitic Chain and on the existence of Man in the Lower Quaternary in this Indochina region]. *C R Acad Sc, Paris* 203:738-741.
7. Fromaget J (1937) Aperçu sur la Stratigraphie et l'Anthropologie préhistorique des formations récentes dans la Chaîne Annamitique et le Haut-Laos. *C R douzième session du Congrès préhistorique de France, Toulouse-Foix*:785-798. French.
8. Driessen P & Deckers J (2001) World Soil Resources Reports 94. (Rome).
9. Demeter F (2000) *Histoire du peuplement humain de l'Asie extrême-orientale depuis le Pléistocène supérieur récent* [Peopling history of the humans in Far East Asia since the Late Upper Pleistocene]. Ph.D. doctorate (University of Paris, Paris, France). French.
10. Wang H, *et al.* (2003) Pyrolysis combustion ¹⁴C dating of soil organic matter. *Quat Res* 60:348-355.
11. Rink WJ, Rendell H, Marseglia EA, Luff BJ, & Townsend PD (1993) Thermoluminescence spectra of igneous quartz and hydrothermal vein quartz. *Phys Chem Min* 20(5):353-361.
12. Kuhn R, *et al.* (2000) A study of thermoluminescence emission spectra and optical stimulation spectra of quartz from different provenances. *Radiat Meas* 32(5-6):653-657.

13. Tan K, *et al.* (2009) Three-dimensional thermoluminescence spectra of different origin quartz from Altay Orogenic belt, Xinjiang, China. *Radiat Meas* 44(5-6):529-533.
14. Gotze J (2009) Chemistry, textures and physical properties of quartz - geological interpretation and technical application. *Mineralog Mag* 73(645-671).
15. Westaway KE & Prescott J (2012) A new light on quartz origins: the link between geology and spectra. *Radiat Meas* under review.
16. Aitken MJ (1998) *An Introduction to Optical Dating* (Oxford University Press, Oxford).
17. Huntley DJ, Godfrey-Smith DI, & Thewalt MLW (1985) Optical dating of sediments. *Nature* 313(5998):105-107.
18. Duller GAT (2004) Luminescence dating of Quaternary sediments: recent advances. *J Quat Sci* 19(2):183-192.
19. Stokes S (1999) Luminescence dating applications in geomorphological research. *Geomorphol* 29:153-171.
20. Murray AS & Wintle AG (2000) Luminescence dating of quartz using an improved single-aliquot regenerative-dose protocol. *Radiat Meas* 32(1):57-73.
21. Westaway KE & Roberts RG (2006) A dual-aliquot regenerative-dose protocol (DAP) for thermoluminescence (TL) dating of quartz sediments using the light-sensitive and isothermally stimulated red emissions. *Quat Sci Rev* 25(19-20):2513-2528.
22. Morwood MJ, *et al.* (2004) Archaeology and age of a new hominin from Flores in eastern Indonesia. *Nature* 431(7012):1087-1091.
23. Morwood MJ, *et al.* (2005) Further evidence for small-bodied hominins from the Late Pleistocene of Flores, Indonesia. *Nature* 437(7061):1012-1017.
24. Hashimoto T, Hayashi Y, Koyanagi A, Yokosaka K, & Kimura K (1986) Red and blue coloration of thermo-luminescence from natural quartz sands. *Nucl Tracks Radiat Meas* 11(4-5):229-235.
25. Hashimoto T, Yokosaka K, & Habuki H (1987) Emission properties of thermo-luminescence from natural quartz - blue and red TL response to absorbed dose. *Nucl Tracks Radiat Meas* 13(1):57-66.
26. Fattahi M & Stokes S (2000) Red thermoluminescence (RTL) in volcanic quartz: development of a high sensitivity detection system and some preliminary findings. *Ancient TL* 18:35-55.
27. Scholefield RB & Prescott JR (1999) The red thermoluminescence of quartz: 3-D spectral measurements. *Radiat Meas* 30(1):83-95.
28. Scholefield RB, Prescott JR, Franklin AD, & Fox PJ (1994) Observations on some thermoluminescence emission centers in geological quartz. *Radiat Meas* 23:409-412.
29. Westaway KE (2009) The red, white and blue of quartz luminescence: A comparison of D(e) values derived for sediments from Australia and Indonesia using thermoluminescence and optically stimulated luminescence emissions. *Radiat Meas* 44(5-6):462-466.

30. Westaway KE (2006) Reconstructing the Quaternary landscape evolution and climate history of western Flores: an environmental and chronological context for an archaeological site. (University of Wollongong, Wollongong).
31. Westaway KE & Prescott J (2012) Investigating signal evolution: a comparison of red and blue signals emitted by the same quartz sample. *Radiat Meas* under review.
32. Spooner NA & Franklin AD (2002) Effect of the heating rate on the red TL of quartz. *Radiat Meas* 35(1):59-66.
33. Murray AS & Mejdahl V (1999) Comparison of regenerative-dose single-aliquot and multiple-aliquot (SARA) protocols using heated quartz from archaeological sites. *Quat Sci Rev* 18(2):223-229.
34. Huot S, Buylaert JP, & Murray AS (2006) Isothermal thermoluminescence signals from quartz. *Radiat Meas* 41(7-8):796-802.
35. Yoshida H, Roberts RG, & Olley JM (2003) Progress towards single-grain optical dating of fossil mud-wasp nests and associated rock art in northern Australia. *Quat Sci Rev* 22(10-13):1273-1278.
36. Morwood MJ, *et al.* (2009) Preface: research at Liang Bua, Flores, Indonesia. *J Hum Evol* 57(5):437-449.
37. Roberts RG, *et al.* (2009) Geochronology of cave deposits at Liang Bua and of adjacent river terraces in the Wae Racang valley, western Flores, Indonesia: a synthesis of age estimates for the type locality of *Homo floresiensis*. *J Hum Evol* 57(5):484-502.
38. Roberts R, *et al.* (1998) Optical and radiocarbon dating at Jinmium rock shelter in northern Australia. *Nature* 393(6683):358-362.
39. Botter-Jensen L, Bulur E, Duller GAT, & Murray AS (2000) Advances in luminescence instrument systems. *Radiat Meas* 32(5-6):523-528.
40. Olley JM, Roberts RG, Yoshida H, & Bowler JM (2006) Single-grain optical dating of grave-infill associated with human burials at Lake Mungo, Australia. *Quat Sci Rev* 25(19-20):2469-2474.
41. Jacobs Z, Duller GAT, & Wintle AG (2006) Interpretation of single grain D-e distributions and calculation of D-e. *Radiat Meas* 41(3):264-277.
42. Botter-Jensen L, Andersen CE, Duller GAT, & Murray AS (2003) Developments in radiation, stimulation and observation facilities in luminescence measurements. *Radiat Meas* 37(4-5):535-541.
43. Olley JM, *et al.* (2004) Optical dating of deep-sea sediments using single grains of quartz: a comparison with radiocarbon. *Sediment Geol* 169(3-4):175-189.
44. Westaway KE, *et al.* (2007) Age and biostratigraphic significance of the Punung Rainforest Fauna, East Java, Indonesia, and implications for *Pongo* and *Homo*. *J Hum Evol* 53(6):709-717.
45. Galbraith RF, Roberts RG, Laslett GM, Yoshida H, & Olley JM (1999) Optical dating of single and multiple grains of quartz from Jinmium rock shelter, northern Australia, part 1, Experimental design and statistical models. *Archaeometry* 41:339-364.

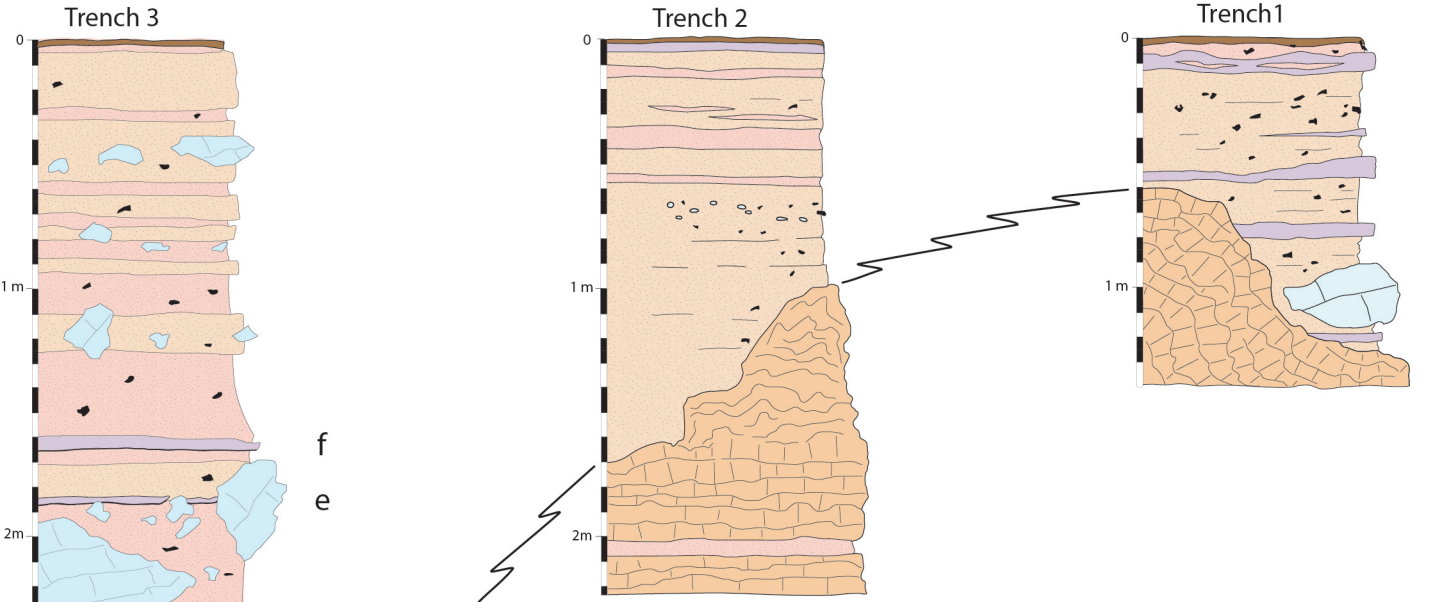
46. Rodnight H, Duller GAT, Wintle AG, & Tooth S (2006) Assessing the reproducibility and accuracy of optical dating of fluvial deposits. *Quat Geochronol* 1(2):109-120.
47. Stokes S, *et al.* (2003) Alternative chronologies for Late Quaternary (Last Interglacial-Holocene) deep sea sediments via optical dating of silt-sized quartz. *Quat Sci Rev* 22(8-9):925-941.
48. Mejdahl V (1979) Thermoluminescence dating: beta-dose attenuation in quartz grains. *Archaeometry* 21:61-72.
49. Feathers JK & Migliorini E (2001) Luminescence dating at Katanda - a reassessment. *Quat Sci Rev* 20(5-9):961-966.
50. Prescott JR & Hutton JT (1994) Cosmic-ray contributions to dose-rates for luminescence and ESR dating - large depths and long-term time variations. *Radiat Meas* 23(2-3):497-500.
51. Olley JM, Murray A, & Roberts RG (1996) The effects of disequilibria in the uranium and thorium decay chains on burial dose rates in fluvial sediments. *Quat Sci Rev* 15(7):751-760.
52. Ivanovich M & Harmon RS (1992) *Uranium-series disequilibrium: applications to earth, marine and environmental sciences* (Clarendon Press, Oxford).
53. Olley JM, Roberts RG, & Murray AS (1997) Disequilibria in the uranium decay series in sedimentary deposits at Allen's Cave, Nullarbor Plain, Australia: Implications for dose rate determinations. *Radiat Meas* 27(2):433-443.
54. Southon JR (2007) Graphite reactor memory - where is it from and how to minimize it? *Nucl Instr Meth Phys Res B* 259(1):288-292.
55. Stuiver M & Polach HA (1977) Discussion: Reporting of ^{14}C data. *Radiocarbon* 19:5-363.
56. Reimer PJ, *et al.* (2009) IntCal09 and Marine09 Radiocarbon Age Calibration Curves, 0-50,000 Years cal BP. *Radiocarbon* 51.
57. Hughen K, Southon J, Lehman S, Bertrand C, & Turnbull J (2006) Marine-derived ^{14}C calibration and activity record for the past 50,000 years updated from Cariaco Basin. *Quat Sci Rev* 25:3216-3227.






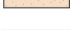





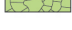





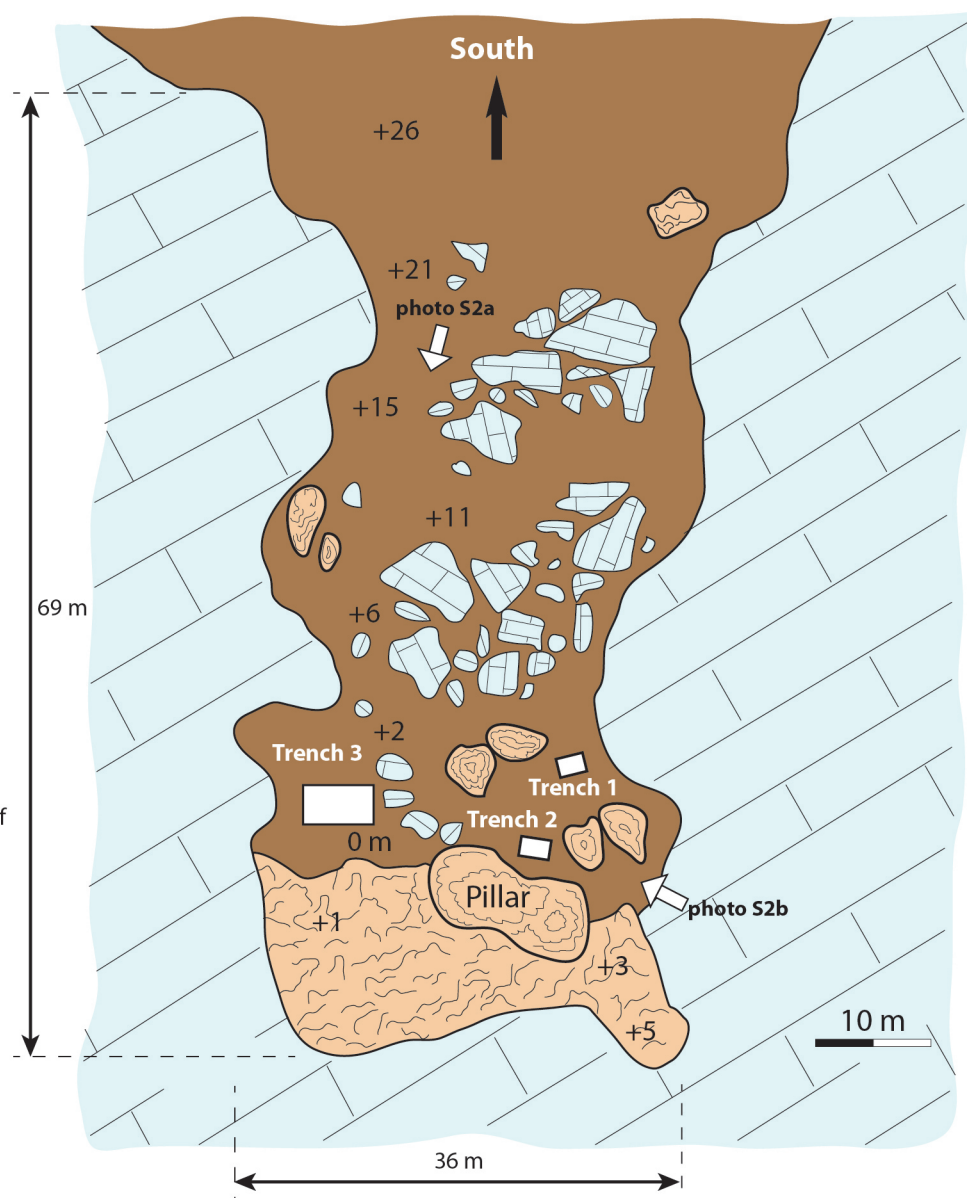


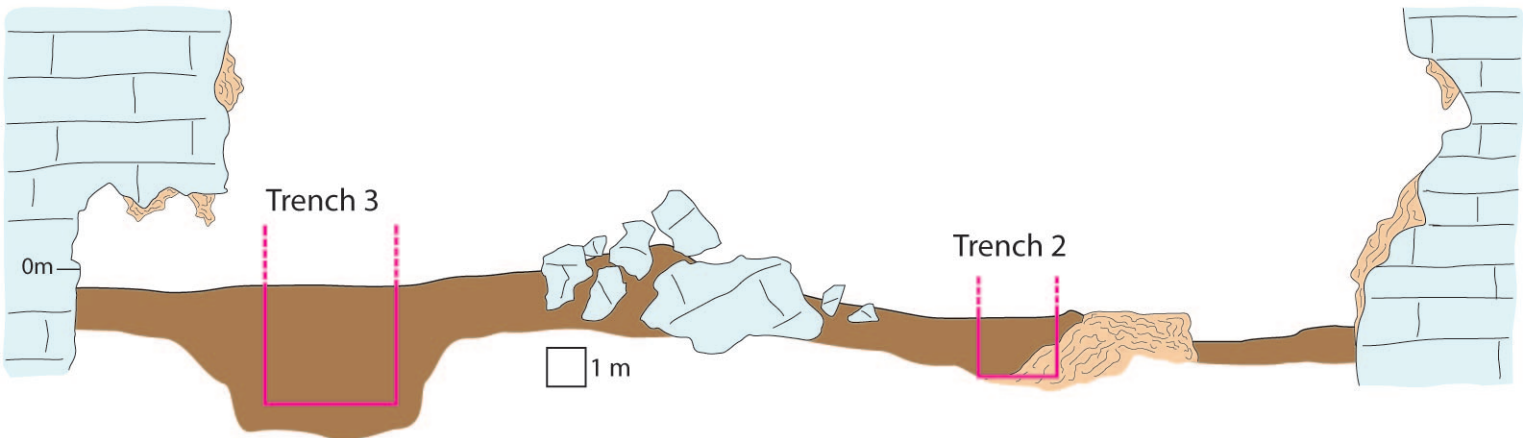
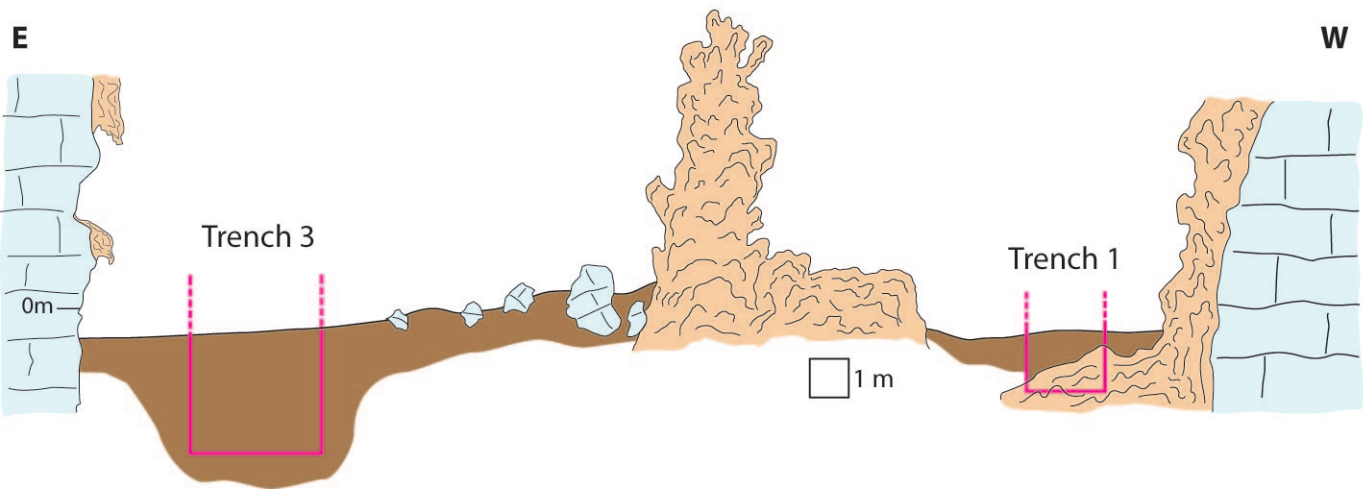


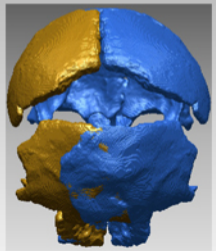
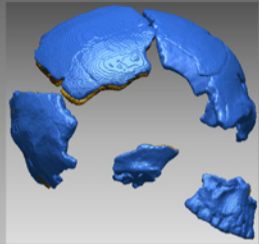
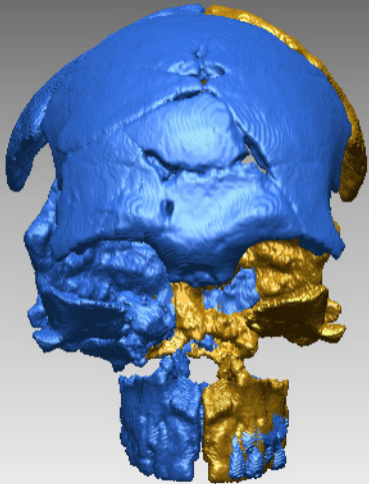
f
e
d
c
b
a

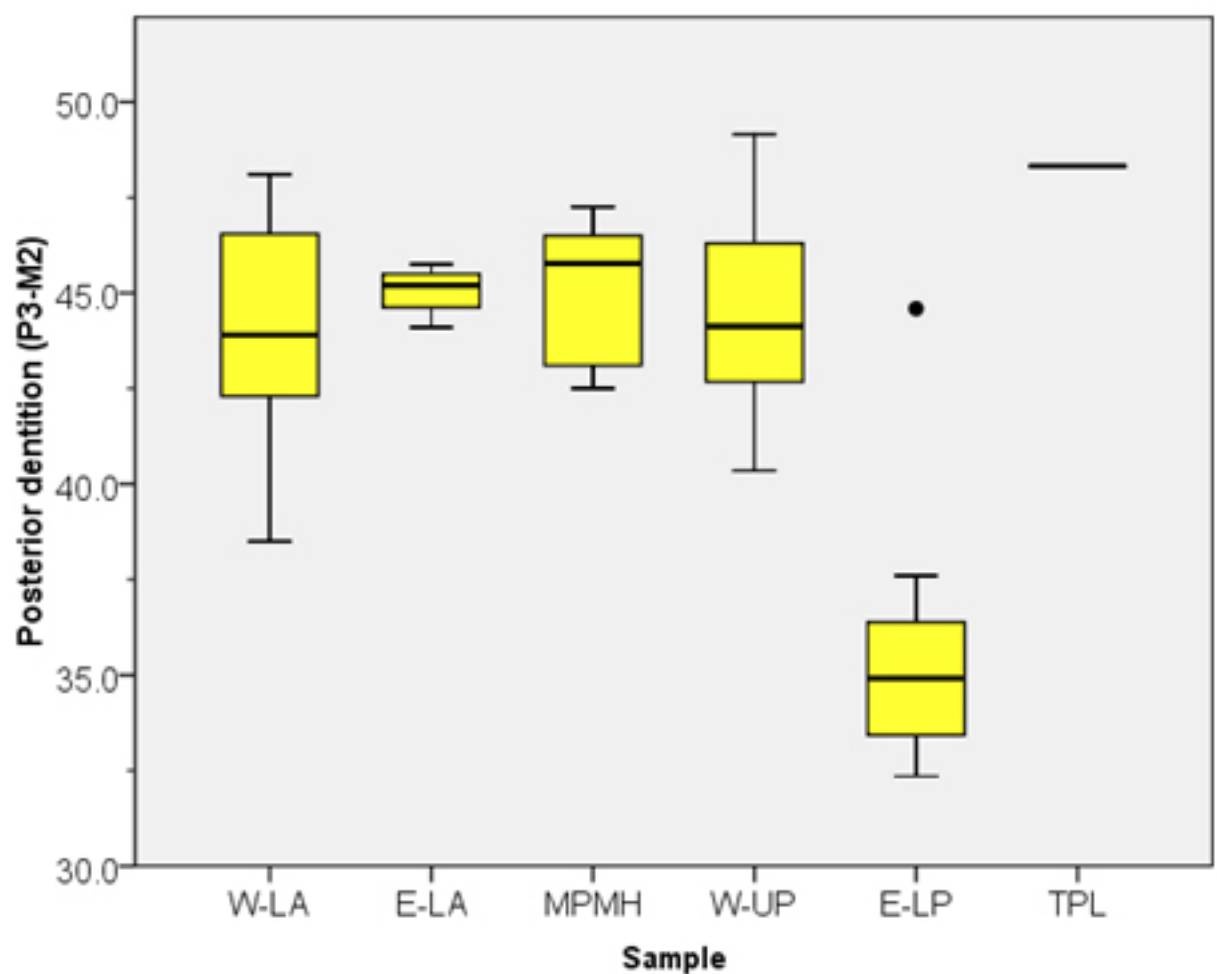
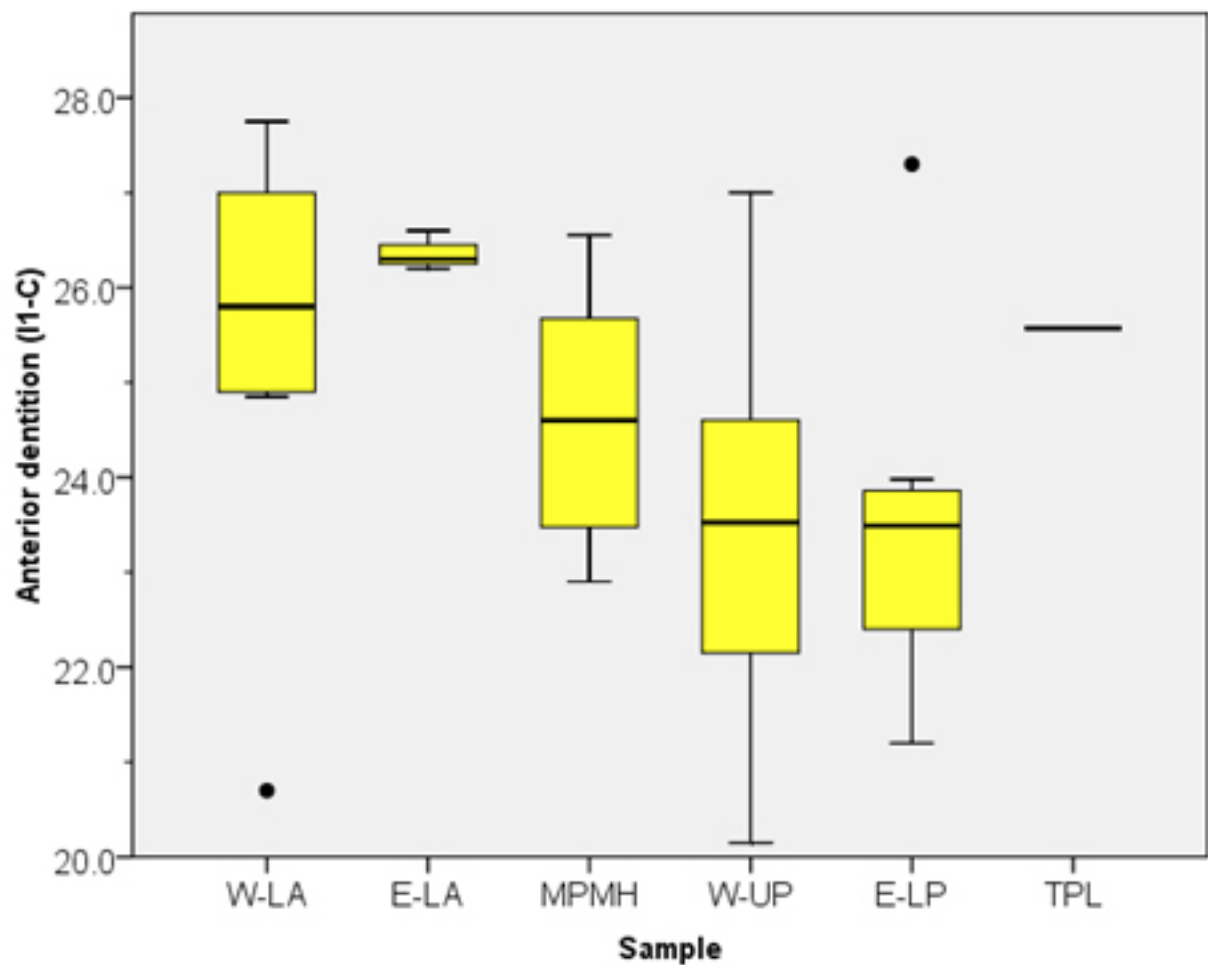
-  Limestone substratum
-  Silty clays
-  Sandy clays
-  Speleothems
-  Calcite-rich white silty clays with powdery limestone precipitate
-  Limestone blocs collapsed from roof
-  Reworked speleothems
-  Charcoal
-  Clays from cave floor
-  Skull
-  Trench

0 m, +2 Ground elevation compared to zero level from trench 3



ESE**WNW****E****W**





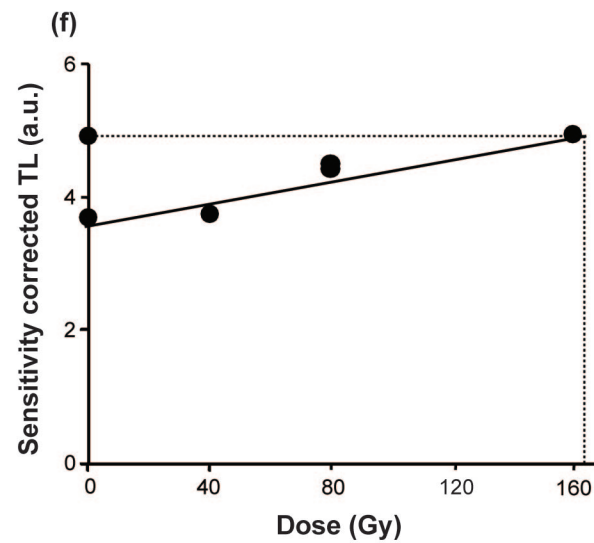
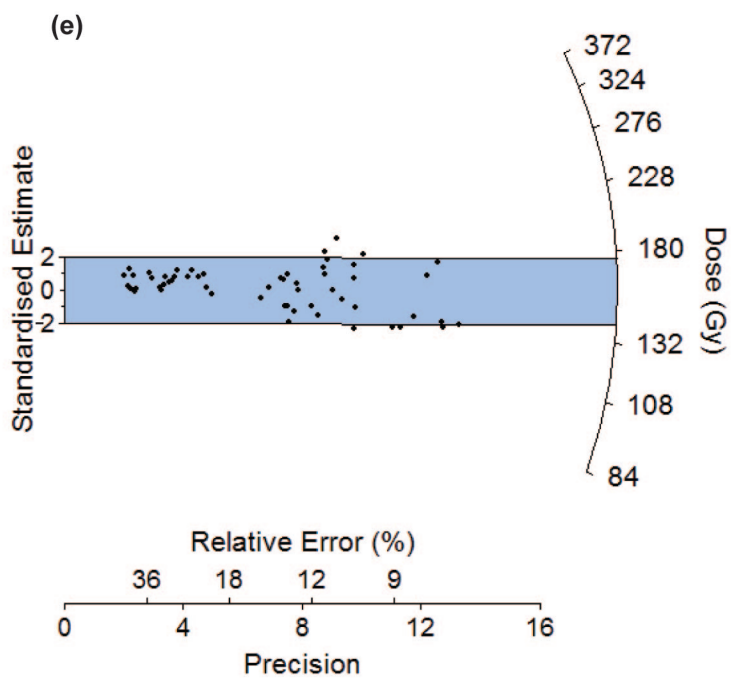
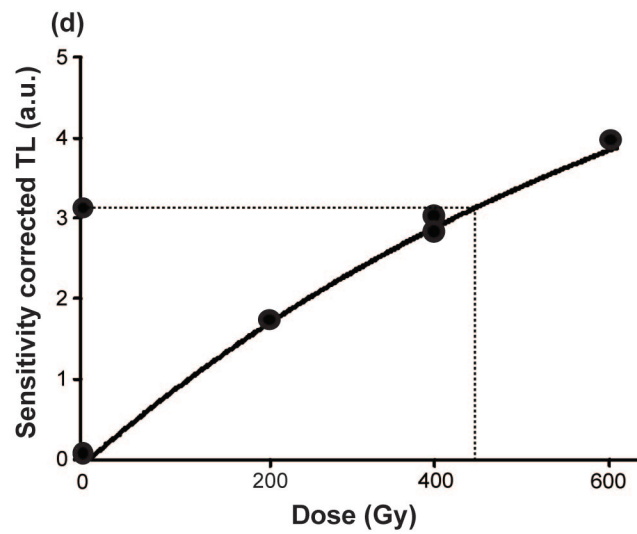
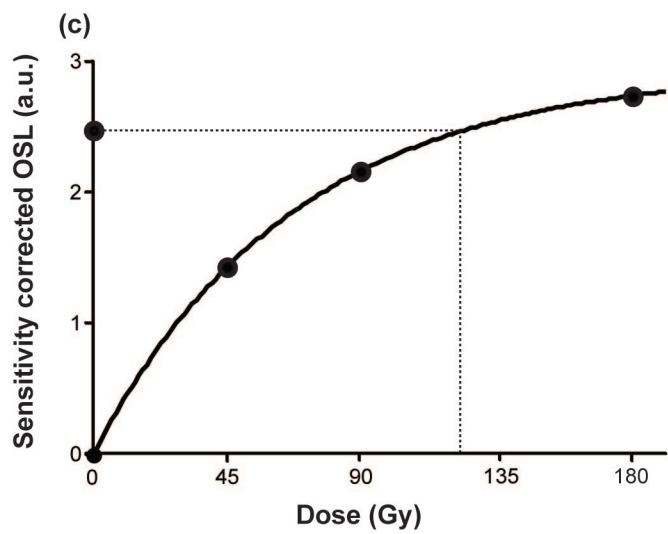
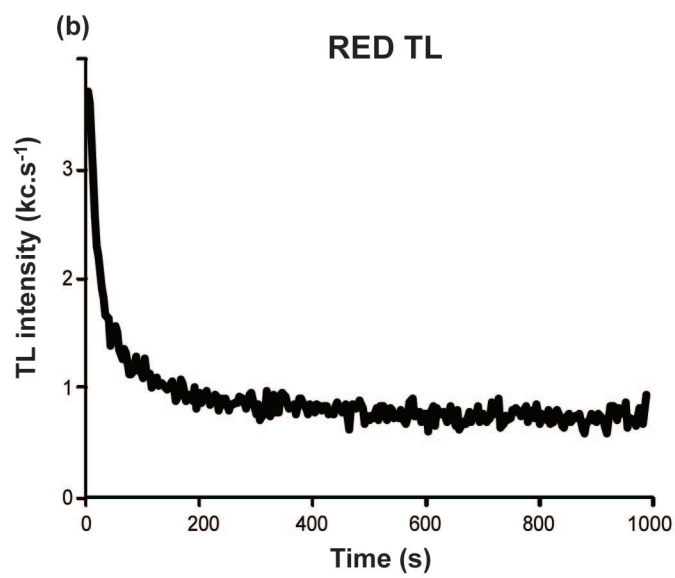
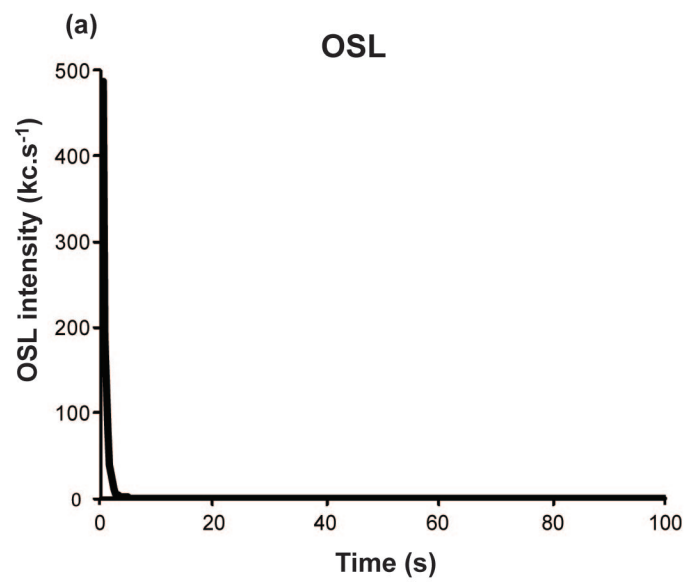
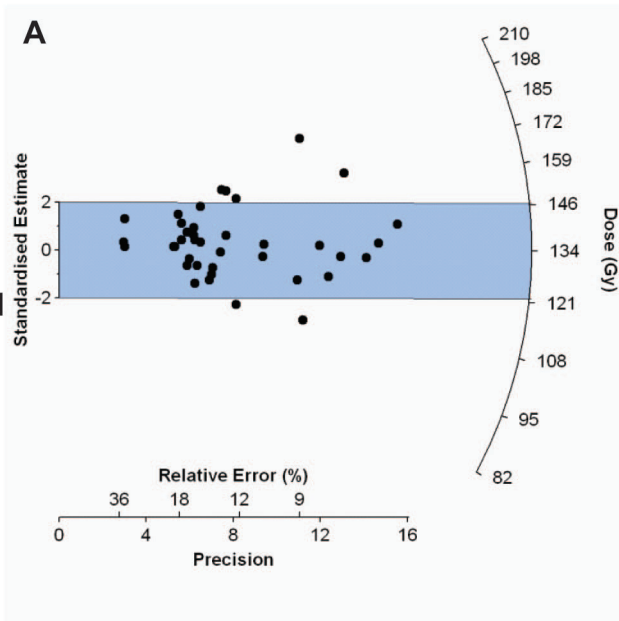


Fig S2

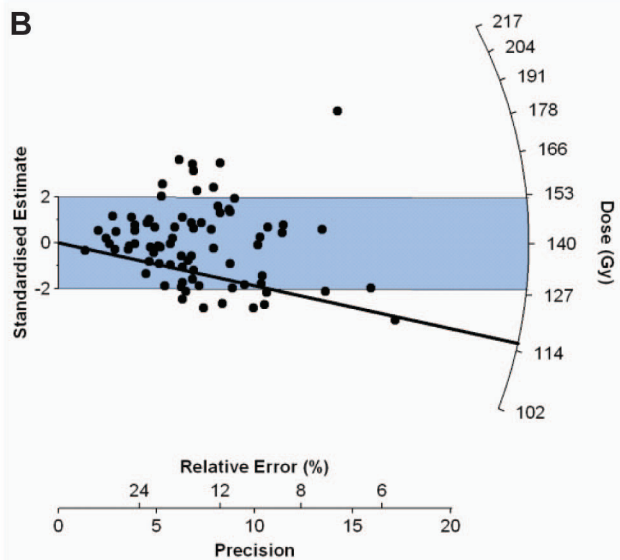
SINGLE-ALIQUOT

TPL-1



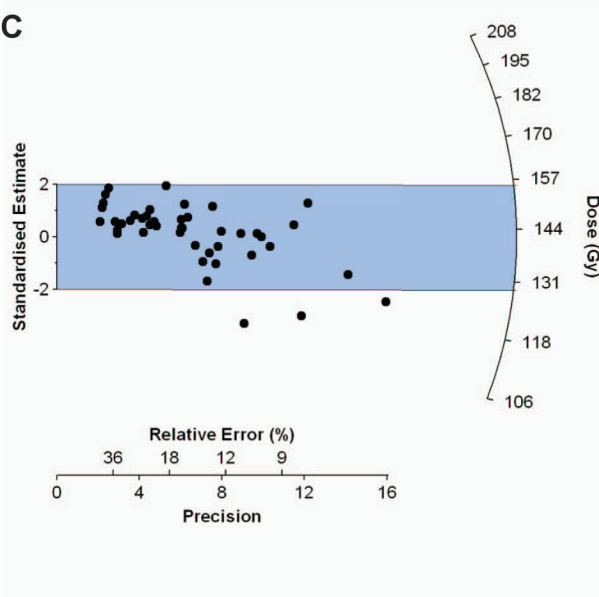
SINGLE-GRAIN

B

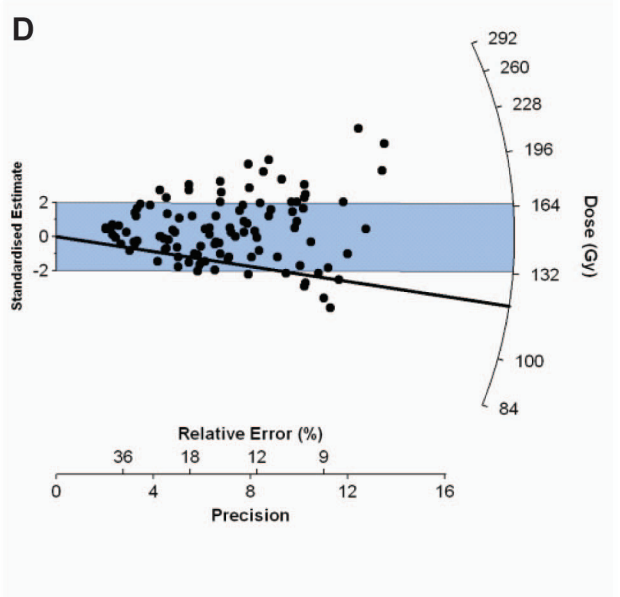


TPL-2

C

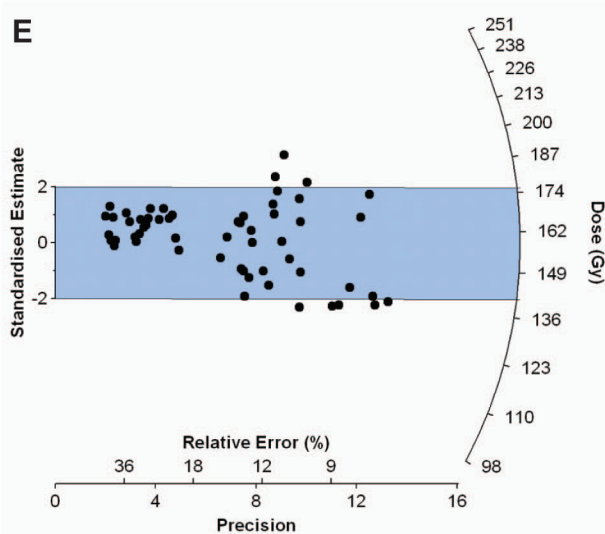


D

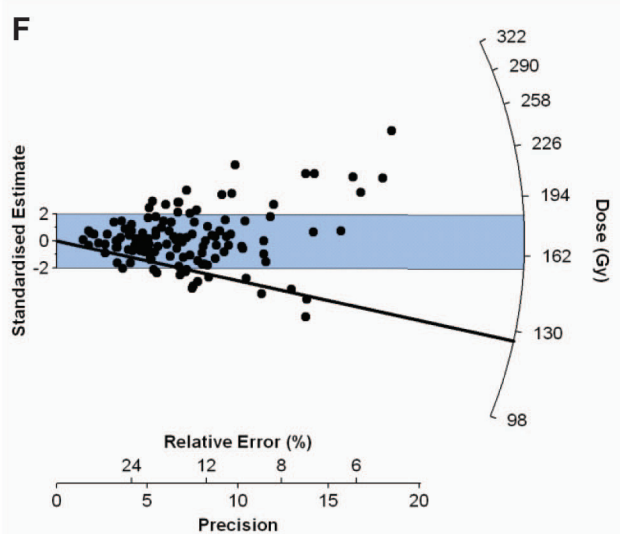


TPL-3

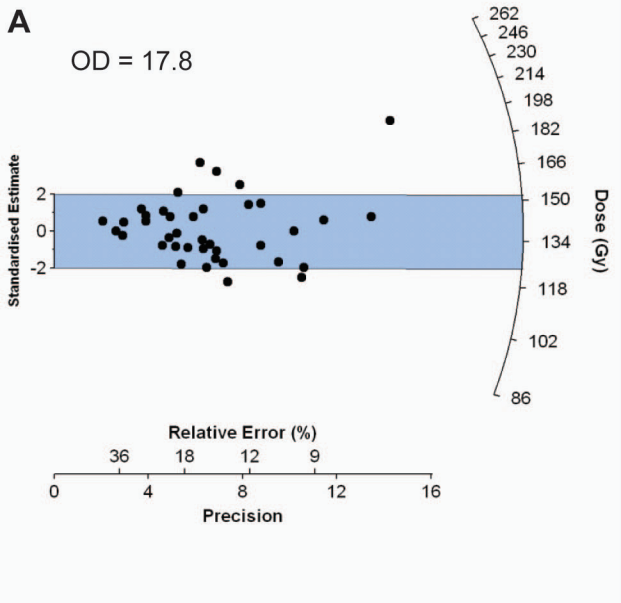
E



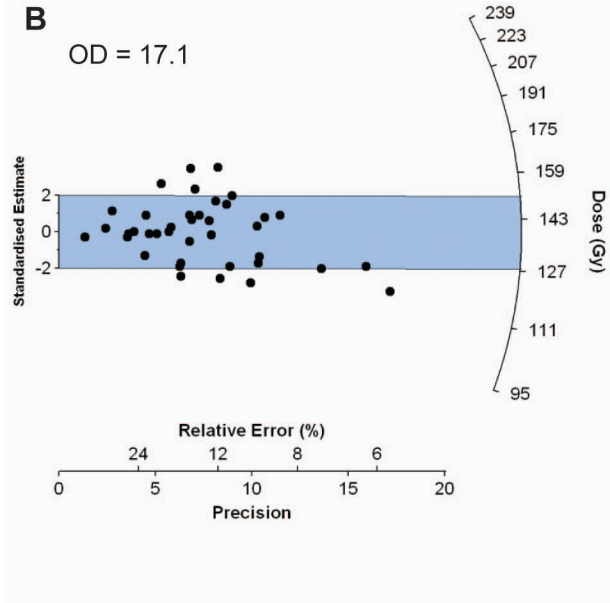
F

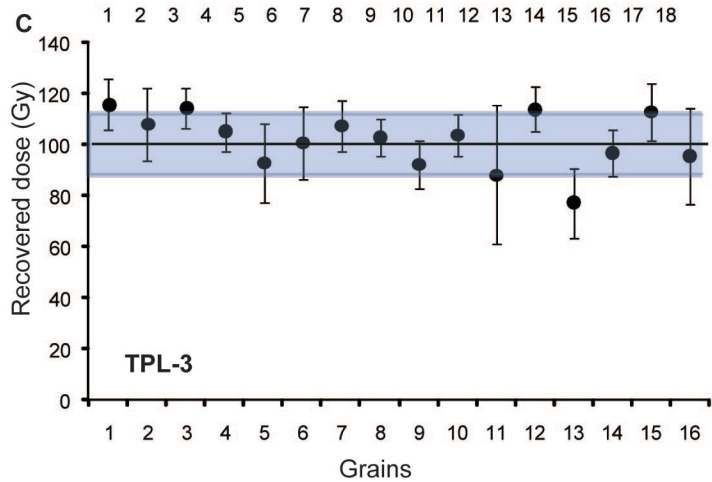
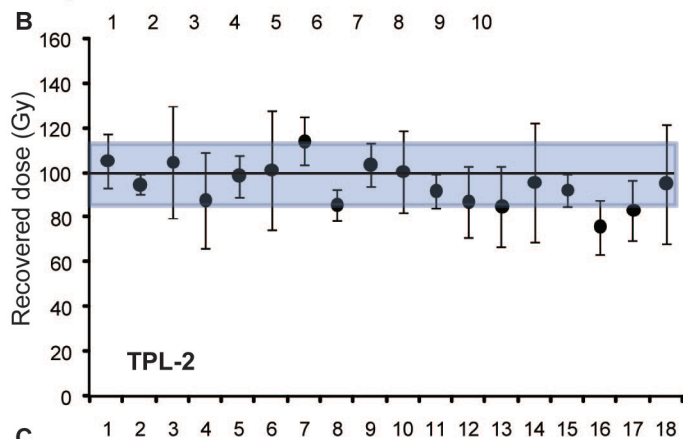
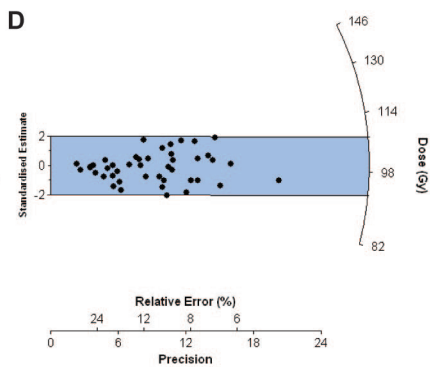
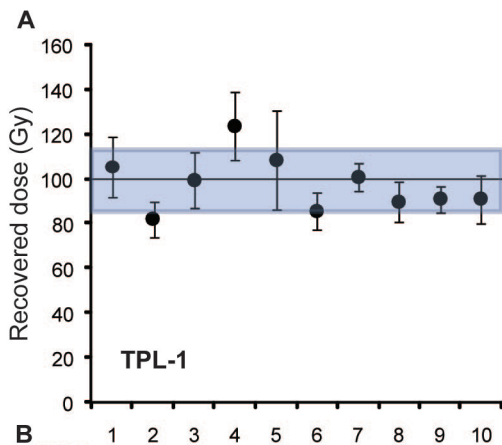


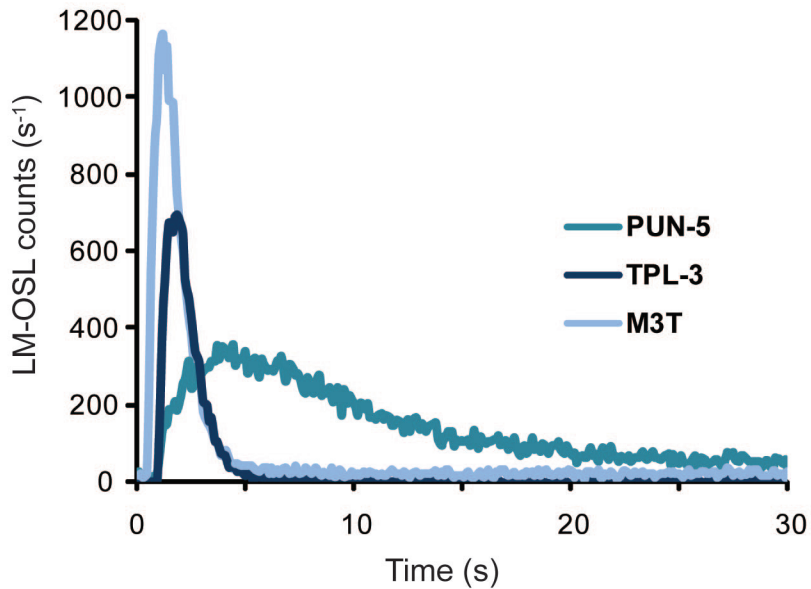
GLOUCESTER UNIVERSITY - UK



MACQUARIE UNIVERSITY - AUST







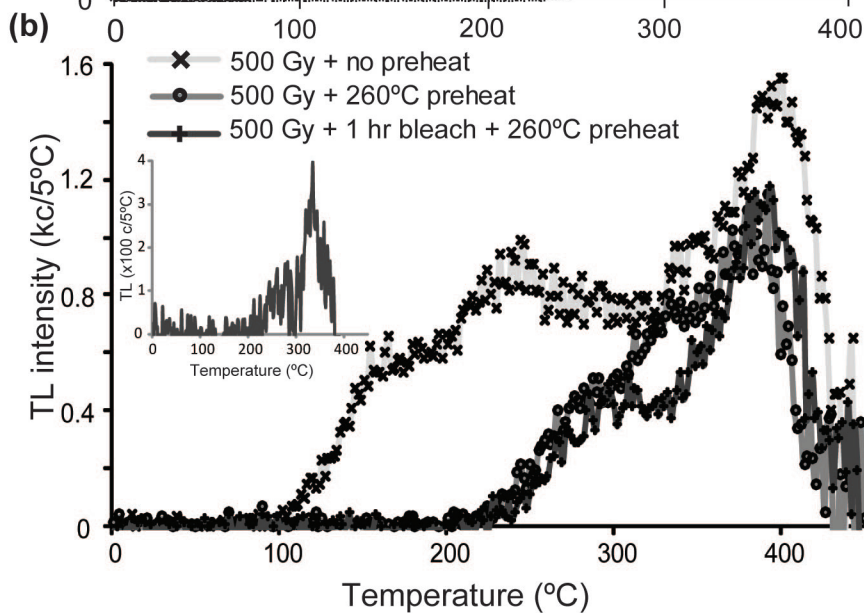
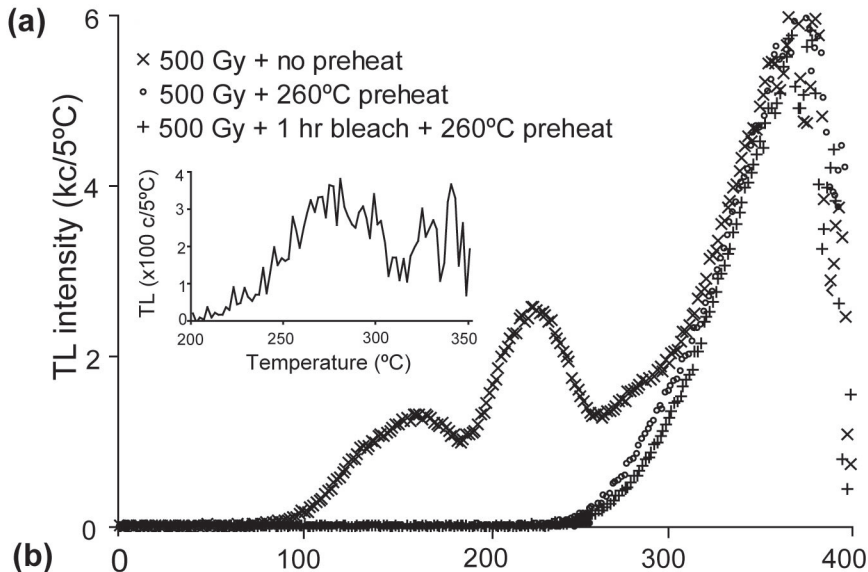


Table S1. Radiocarbon dating of four charcoal samples retrieved from TPL as shown on **Fig. 1** (Radiocarbon Dating Laboratory, Illinois State Geological Survey, University of Illinois at Urbana-Champaign, USA.). The half-life of 5568 is used for age calculation. Ages are reported as BP (before present defined as before 1950).

ISGS Lab Code	Sample	$\delta^{14}\text{C}^3$	\pm	^{14}C yr BP	$\delta^{13}\text{C}$
A1451	TPL 09-1	-132.2	1.3	1,140 \pm 15	-24.1
A1452	TPL 09-2	-291.5	1.0	2,770 \pm 15	-23.9
A1453	TPL 09-3	-1000.0	1.1	> 49,200	-26.6
A1291	TPL b	-998.3	0.7	51,400 \pm 3,300	-24.8

Table S2. U-Th dating of TPL 1¹ (Department of Geology, University of Illinois at Urbana-Champaign, USA).

Sample	U (ppm)	$^{234}\text{U}/^{238}\text{U}$	$^{230}\text{Th}/^{232}\text{Th}$	Age (ka BP) Detrital corr.	Error
DEM	18.3	2.552 \pm 0.006	318.0 \pm 3.0	63.6	6.0

¹ The sample was dissolved in 8N HNO₃, and isotopic tracers ^{229}Th and ^{236}U were added. The U and Th were separated from the matrix using standard chromatographic methods. U and Th isotopic compositions were determined using a Nu Plasma HR multicollector. The instrument has an abundance sensitivity of < 500ppb at 1 amu. Although analytical precisions on all measured isotope ratios were << 1% (2s) and age correction for an assumed bulk earth detrital correction was negligible, we conservatively assign a 10% error to our measured ages.

Table S3. Cranial measurements for TPL 1 and comparative samples. All measurements in mm. Data given as mean \pm s.d. (N). Samples are as follows: W-LA: Western Eurasian late archaic humans; E-LA: Eastern Eurasian late archaic humans; MPMH: Middle Paleolithic modern humans; W-UP: Western Eurasian Upper Paleolithic humans; E-LP: Eastern Eurasian Late Pleistocene humans. For additional information on sample composition see SI.

	TPL 1	W-LA	E-LA*	MPMH	W-UP	E-LP
Min frontal breadth (M-9)	96.0	105.2 \pm 4.4 (16)	109 ²	102.4 \pm 4.9 (6)	100.7 \pm 4.4 (28)	95.3 \pm 6.5 (18)
Max frontal breadth (M-10)	106.0 ¹	122.4 \pm 5.8 (15)	117.7 ²	119.4 \pm 4.2 (5)	121.8 \pm 5.5 (33)	117.0 \pm 6.7 (17)
Frontal arc (M-26a)	134.0	124.5 \pm 8.4 (15)	134	127.7 \pm 5.9 (6)	134.4 \pm 7.9 (34)	124.3 \pm 9.6 (19)
Frontal chord (M-29)	115.0	113.1 \pm 5.9 (15)	115.6	112.7 \pm 4.4 (6)	115.6 \pm 6.3 (33)	107.8 \pm 7.7 (19)
Nasal breadth (M-54)	28.0	32.0 \pm 3.3 (18)	28.5 ²	31.2 \pm 1.2 (5)	25.8 \pm 2.1 (26)	26.7 \pm 2.7 (6)

*Frontal bone data is for Maba 1; nasal breadth data is for Changyang.

¹ Maximum frontal breadth of TPL 1 may be slightly underestimated due to damage to the frontal bone.

² Measurement is taken from the preserved side and multiplied by two.

Table S4. Maxillary crown dimensions of TPL 1 in mm.

Tooth	Side	BL^a	MD^b	A^c
I ¹	R	7.44	9.10	2
I ²	R	7.53	7.24	2
	L	6.88	7.36	2
C	R	10.60	9.24	1
	L ^d	9.18	8.64	1
P ³	R	11.57	8.05	1
	L ^d	10.13	7.70	1
P ⁴	R	10.82	7.30	1
	L ^d	11.20	7.73	1
M ¹	R	12.68	11.10	1
	L	--	12.21	2
M ²	R	13.25	11.00	0-1

^a BL: buccolingual crown diameter.

^b MD: mesiodistal crown diameter. These dimensions may be reduced due to interproximal wear.

^c A: Wear state (Arizona State University Dental Anthropology System).

^d Dental dimensions may be expanded due to sediment-filled fissures.

Table S5. Red TL multiple estimate results.

Sample	Original D_e	Number of multiple estimations	Range of D_e values (Gy)	Standard deviation	MAM applied to multiple estimates
TPL-1	137 ± 26	12	92-180	35 ± 9	130 ± 29
TPL-2	144 ± 43	12	108-185	32 ± 9	136 ± 40
TPL-3	165 ± 70	12	101-235	42 ± 15	154 ± 33

Table S6. OSL Single-aliquot rejections.

Sample	Single-aliquots processed	Single-aliquots rejected	Single-aliquots accepted	Overdispersion (%)	Statistical model used
TPL-1	48	11	37	15.6	MAM
TPL-2	48	4	44	10.1	MAM
TPL-3	65	9	56	11.8	MAM

Table S7. OSL Single-grain rejections.

Sample	Single grains processed	Single grains rejected	Single grains accepted	Proportion of luminescence emitting grains	Rejection rate (%)	Over-dispersion (%)	Statistical model
TPL-1	1200	1121	79	6.6	93.4	18.8	MAM
TPL-2	1200	1094	106	8.8	91.2	19.8	MAM
TPL-3	1200	1076	124	10.3	89.7	21.2	MAM

Criteria	TPL-1	TPL-2	TPL-3
Signal $>3\sigma_{BG}$	901	799	805
Recycling ratio $>10\%$ unity	109	163	156
IR ratio $IR >2\sigma$ signal	23	21	32
Supersaturating grains	47	72	54
Recuperation $>5\%$	11	8	9
Ultrafast	5	5	3
Excessive sensitivity change	12	12	9
Desensitizing slow component	6	14	8
Dominance of medium component	7	0	0